Version of Record: https://www.sciencedirect.com/science/article/pii/S0029549322004885
Manuscript_489d376a06c6099f5673d0f21a9f0705

Experimental Validation of Simplified Radionuclide Transport Bubble Scrubbing Code in Sodium Coolant Pool

Kyle F. Becker and Mark H. Anderson

Abstract – Solid radionuclides released following fuel pin failure may become entrained in gaseous fission products and be rapidly transported through the coolant pool to the cover gas region. Sensitivity studies on radionuclide transport have identified this potential pathway as one of both high concern and high uncertainty. The simplified radionuclide transport scrubbing code utilizes classical aerosol scrubbing mechanisms to model this phenomenon and predict aerosol masses reaching the cover gas region. This paper serves to validate this code in a sodium environment while conducting a parametric study to analyze the effects of aerosol size, bubble size, pool temperature, pool depth, aerosol density, and aerosol concentration. Through a series of experimental tests, it was determined that aerosol sizes ranging from 0.001 to 1.0 micron are of primary concern as aerosols in this range have a ratio of aerosol mass entering the sodium pool from the fuel pin to aerosol mass exiting the sodium pool to the cover gas region of less than 10. The experimental results were found to match the trends found in the scrubbing model closely, but significantly more scrubbing was seen experimentally. Decreasing bubble size and increasing pool depth and aerosol density were all found to increase scrubbing both experimentally and theoretically. Pool temperature was found to have a negligible effect on scrubbing amounts; however, this was largely due to a subsequent increase in bubble size corresponding to increasing temperatures which offset the increase in scrubbing due to increased temperature. Varying aerosol concentration was found to have no effect on scrubbing ratios. A final series of tests was conducted for a more prototypic fuel pin failure with a heterogenous bubble swarm. From these tests, it was found that the experimental scrubbing quantities were larger than for the single bubble case. Overall, it was found that the simplified bubble transport scrubbing code accurately models the trends of the bubble scrubbing but provides a conservative estimate of scrubbing quantities. Model limitations fail to model the complex phenomena present for fission product scrubbing via bubble transport, but match trends seen experimentally.

Keywords: Sodium Fast Reactor, Pool Scrubbing, Radionuclides, Decontamination Factor, Aerosols, Source Term

1. Introduction

With focus on developing generation IV nuclear reactors, sodium fast reactors (SFRs) have received renewed interest (Flanagan *et al.*, 2015). SFRs have many inherent benefits when compared to light water reactors (LWRs), such as improved efficiencies, drastically greater margins to boiling, close to atmospheric pressures in the cover gas region, and net negative reactivity feedback (Flanagan *et al.*, 2005, 2015; Liu and He, 2019). However, prior to commercial deployment of these reactors, licensing from the Nuclear Regulatory Commission (NRC) must be obtained. Historically, this licensing process has required bounding, conservative, deterministic models to predict source terms following accident scenarios. With

advances in computer processing power and technical knowledge, a more realistic, mechanist model can now be used (Grabaskas *et al.*, 2015). Research at Argonne National Laboratory (ANL) has been conducted to identify technology gaps hindering the development of a mechanistic source term. From this, three major gaps in knowledge were found in bubble transport, in-pin migration and release, and aerosol behavior (Grabaskas *et al.*, 2015, 2016). In-pin migration is the transport of fission products from the fuel matrix up to the upper plenum of the fuel pin. Fission product retention via bubble transport, in particular, was found to be of very high importance in determining the overall source term. In addition, the large uncertainties in this phenomenon make fission product retention via bubble transport a key area of interest in the overall radionuclide (RN) transport model (Grabaskas *et al.,* 2016).

In a theorized fuel pin failure, cladding breaches in both the upper plenum and fuel sections of the fuel pin may results in an expulsion of RN inventory from the fuel pin into the surrounding coolant pool. Gaseous fission products are expected to rise quickly through the pool with little to no solubility within the sodium pool, in accordance with Henry's law (Thormeier, 1970). Overall retention of all other solid and liquid fission products is expected to be high (Grabaskas *et al.*, 2016). However, liquid and solid fission products may become entrained in gaseous fission products upon injection into the sodium pool and be transported directly to the cover gas region, bypassing the coolant pool. The ratio of fission products initially entrained in the bubble to those transported to the cover gas region can be defined as the decontamination factor (DF).

Fission product retention via bubble transport is of concern in various pool type reactor designs. Considerable research has been conducted to better understand this phenomenon in water coolant pools (Dehbi, 2001 *et al.*; Hakii and Kaneko, 1990; Kanai *et al.*, 2016; Kaneko *et al.*, 1992; Li *et al.*, 2019; Yoshida and Fujiwara, 2021). From these studies, it was found that the parameters of pool depth, particle size, and gas flow velocity had the greatest effect on the DF. Particle size in particular was found to be of critical importance due to distinct decrease in DF between the sizes of approximately 0.01 to 1.0 micron (i.e. low amounts of scrubbing between these sizes and nearly complete scrubbing outside of these sizes). Historically, there has been limited research regarding fission product retention via bubble transport in a molten sodium pool. Most notable, work by Miyahara in the 90s focused on iodine scrubbing from a mixed xenon-iodine gas bubble in a sodium pool (Miyahara *et al.*, 1996). In this study, a quartz sphere was ruptured in a liquid sodium pool and the subsequent iodine scrubbing from the bubble was measured. The iodine which was transported through the pool was collected through an inverted funnel and deposited on aerosol sampling filters. Key parameters such as bubble volume, iodine concentration, pool temperature, and pool depth were varied to study each's respective effects on overall scrubbing. However due to key scrubbing parameters not being examined, most notably particle size, data from this experiment has limited use in validating mechanistic models.

A large amount of work has been conducted with regards to bubble scrubbing models (Kanai *et al.*, 2016; Powers and Sprung, 1993; Pradeep and Sharma, 2019; Wassel *et al.*, 1985). All of these models function off the same classical aerosol principles outlined by Fuchs (1964). When comparing between sodium and water pool types, the main differences in models are the physical properties entered; the same models for particle motion are utilized, however the empirical

correlations used need validation in a sodium environment. When attempting to validate these models to existing experimental results, a general agreement is found. However, all theoretical models assume a single isolated bubble rising in the coolant pool while all aforementioned experimental testing were conducted with various interacting bubbles in a bubble swarm flow regime. This disconnect makes it difficult to directly compare the two results.

This paper builds off work previously conducted in a water column apparatus (Becker and Anderson, 2021) to validate the bubble transport portion of the Simplified Radionuclide Transport (SRT) source term code developed at ANL. In this testing, a TOPAS SAG 410/U Solid Aerosol Generator was used to aerosolize aluminum and nickel powders in a dry air gaseous flow. A series of solenoid valves were used to inject a single isolated bubble into the water pool. The bubble was then allowed to rise uninterrupted through the pool to the cover gas region. Once in the cover gas region, the aerosols which were transported through the pool were collected in cross flow and directed through an inverted nozzle collection system to a (Micro Orifice Uniform Deposit Impactor) MOUDI cascade impactor. The cascade impactor was then able to separate the aerosol particles based on aerodynamic particle size. Amounts deposited were then compared to the calibrated injection amounts to determine the overall DF by particle size. In addition to particle size, bubble size, aerosol density, pool depth, and aerosol concentration were also varied independently to study their respective importance. From this water testing, it was found that as bubble size increased, the DF decreased slightly due to a surface area to volume ratio decreasing with bubble size and the rise velocity increasing with bubble size. Increased aerosol density was shown to have negligible effects at relatively small particle sizes and a significant effect for particle sizes of approximately 1 micron. Increasing pool depth was found to increase scrubbing due to a longer residence time in the pool. Changing aerosol concentration was found to have a negligible effect on overall scrubbing. A final test series was conducted with a sparging device to generate a heterogenous bubbly flow regime. Comparing the results of the bubble swarm testing to that of a single, isolated bubble, it was found that there is increased scrubbing in a bubble swarm due to bubble-to-bubble interactions. When compared to the SRT bubble transport code, the experimental results match the trends well, but had considerably more scrubbing than predicted by the code. Overall, it was found that the SRT code provides a conservative estimate of the experimental results (Becker and Anderson, 2021). This paper expands upon this work by replacing the water with sodium, but utilizes many of the same instrumentation and testing methodology.

2. Simplified Radionuclide Transport Bubble Model

The SRT model is designed for source term assessment for pool-type, metal fuel SFR designs. The SRT code is able to rapidly perform uncertainty and sensitivity analyses to determine RN inventories in various containment levels (Bucknor, 2017). The code is functional from in-pin RN migration up to offsite dispersion and doses. The subsection of the SRT code concerned with RN bubble transport is of primary concern with this paper. The bubble transport section is operational with two settings: a simple bubble model and a detailed bubble model. The simple bubble model utilizes a user defined DF to determine amounts of RN entering the cover gas region. The detailed bubble model, on the other hand, utilizes classical aerosol scrubbing theory to predict the amounts of RNs reaching the cover gas region. The scrubbing mechanisms utilized

are Brownian diffusion, inertial deposition, gravitational sedimentation, and condensation. More complex scrubbing methods, such as thermophoresis and diffusiophoresis are not considered. Additionally, complex bubble phenomena such as jet flow, bubble agglomeration, bubble shattering, and bubble swarms are not considered (Bucknor *et al.*, 2017). Instead, the bubble is treated as a single isolated bubble. Each removal mechanism is treated independent, and the total particle removal rate is found as the product of the four mechanisms.

The rate constant for scrubbing by Brownian diffusion is defined by Eq. (1):

$$\alpha_D = 6\sqrt{\frac{8\theta}{\pi U_B D_B^3}}\left[\frac{(E^2-1)F(E)}{1+\sqrt{4+2(E^2-1)}}\right] \tag{1}$$

Where θ and $F(E)$ are defined by Eq. (2) and Eq. (3), respectively:

$$\theta = \frac{KT_B C}{3\pi\mu_g d_a} \tag{2}$$

$$F(E) = \left[\frac{1.76E^2}{E^2-1} - \sqrt{2}\right]^{\frac{1}{2}}\left[\frac{E^2\tan^{-1}\left(\sqrt{E^2-1}\right)}{\left(\sqrt{E^2-1}\right)} - 1\right]^{-\frac{1}{2}} \tag{3}$$

As can be seen, Brownian diffusion is heavily dependent both the eccentricity and size of the bubble. Additionally, as Brownian diffusion is inversely proportional to the aerosol diameter, it is predominant for relatively small bubble sizes. Furthermore, Brownian diffusion increases with temperature and decreases with rise velocity. This model for Brownian diffusion, applying Higbie's penetration theory, has been criticized for its oversimplifications resulting in a significant over-prediction of small particle scrubbing. Mills *et al.* have demonstrated the incompatibility between penetration theory and vortex flow (1988). Further, Motegi *et al.* have demonstrated the nonconservative nature of Higbie's model through Lagranian particle tracking simulations. From these studies, it was shown that Brownian diffusion is considerably overpredicted by Fuchs model (Motegi *et al.,* 2022).

The rate constant for inertial deposition is defined by Eq. (4):

$$\alpha_I = \frac{6U_B\tau G(E)}{D_B^2} \tag{4}$$

Where τ and $G(E)$ are defined by Eq. (5) and Eq. (6) respectively:

$$\tau = \frac{\rho_a d_a^2 C}{18\mu_g} \tag{5}$$

$$G(E) = \frac{E^{\frac{4}{3}}\left[(E^2-1)+(E^2-1)^{\frac{3}{2}}(E^2-2)\tan^{-1}\left(\sqrt{E^2-1}\right)\right]}{\left[\sqrt{E^2-1}-E^2\tan^{-1}\left(\sqrt{E^2-1}\right)\right]^2} \tag{6}$$

Again, it can be seen that inertial deposition is strongly dependent on eccentricity and bubble diameter. Additionally, inertial deposition increases proportionally to the square of particle size. The rate constant for inertial deposition increases with increasing rise velocity despite a lesser

residence time in the coolant pool due to the greater impaction of particle on the bubble walls at higher speeds.

The rate constant for gravitational sedimentation is defined by Eq. (7):

$$\alpha_S = \frac{1.5 g \tau E^{\frac{2}{3}}}{D_B U_B} \tag{7}$$

Increasing eccentricity and decreasing bubble diameter and both increase gravitational sedimentation, though to a lesser extent that the two previously mentioned scrubbing mechanisms. Additionally, sedimentation is proportional to the particle diameter squared, indicating it is predominate at larger particle sizes.

Given the rate constants, the individual DFs can be defined by Eq. (8):

$$DF_i = e^{\alpha_i H_P} \tag{8}$$

As the bubble temperature is assumed to be equal to the pool temperature, the DF for condensation is defined by Eq (9):

$$DF_C = \frac{1}{1 - F} \tag{9}$$

Combined together, the total DF is defined by Eq. (10):

$$DF = DF_I DF_S DF_D DF_C \tag{10}$$

Combining the Brownian diffusion with inertial deposition and gravitational sedimentation results in large amounts of scrubbing for relatively large and small particle sizes. At sizes between 0.01 and 1 micron, however, there is a segment where no scrubbing mechanism is dominant and little scrubbing is observed.

3. Bubble Generation and Visualization

Prior to conducting scrubbing tests, a complete understanding of the morphology, size, and rise velocity of the bubbles was required. Experimental testing of various nozzle designs was used to determine the optimal configuration to limit bubble breakup. From this testing, it was found that a downward, inverted nozzle was able to produce relatively large bubbles with little to no break-up. Two nozzle sizes were utilized to test a wider range of bubble sizes and reduce bubble breakup. Each nozzle was machined in 2.54 cm diameter by 1.27 cm height 316 stainless steel (SS). The inverted funnels each had a 30° angle and had base diameters of 1.47 cm and 1.91 cm. A series of solenoid valves, controlled using LabVIEW 2019 running on a NI cRIO-9024 Real-Time Controller, were throttled at varying time increments to produce varying size bubbles. A pressure buffer tank was incorporated to control inlet conditions and reduce deviation in the bubble sizes generated.

Due to the opaque nature of sodium, radiography was used to analyze bubble morphology. A GE Optima XR220 Portable X-Ray was utilized with its corresponding digital detector. X-rays of rising bubbles were taken with a voltage of 125 keV, a current of 120 mA, and an exposure time of 9ms. A source to object distance (SOD) of 101.6 cm was used with an object to image distance (OID) of 17.8 cm. The OID had to be sufficiently large due to the testing column size

and thermal constraints. The x-ray tube had a focal size of 0.6mm (GE, 2022). The x-ray system was connected to the LabVIEW control to synchronize the timing of bubble generation to x-ray exposures. Due to the relatively long exposure times of each X-ray, a series of tests was conducted to quantify the blur over a range of velocities. This was done utilizing a DigiRad C-980 Optical Chopper with harmonic blades. At a velocity of $0.5\ m/s$, the distortional blur was found to be 3.2% of the measured value. This is much less than would be predicted with an exposure time of $9\ ms$ due to the current peaking for a considerably shorter amount of time than the overall exposure time.

Analysis of x-ray images for bubble size was conducted in ImageJ. 30 images of only sodium in the column were captured prior to each testing series and averaged together to provide a background reading. This reading was then subtracted from each image to isolate the argon bubble. The image was then processed using a deconvolution algorithm to produce a silhouette of the bubble. Due to the large size of the bubbles tested, all were spherically capped in shape. The corresponding equivalent diameter of a spherical bubble was then found according to Eq. (11)

$$d_e = \sqrt{\frac{4A}{\pi}} \tag{11}$$

In addition to bubble sizes, the eccentricities were also determined based on the ratio of the major axis to the minor axis of an elliptical fit. X-ray images were taken at three heights: directly above the injection nozzle, 80.65 cm above the nozzle, and 117.48 cm above the nozzle. The rise time to reach these heights was used to determine the initial rise velocity and the terminal rise velocity. Figure 1 shows a representative bubble, through the stages of post processing.

Experimental findings of bubble morphology, eccentricity, and rise velocity were then compared to theory and existing correlations. Utilizing a bubble regime map, characteristic shape can be found based on the dimensionless Morton and Eötvös numbers (Clift *et al.*, 1978). The Morton number is a function of only fluid properties and is defined by Eq. (12):

$$M = \frac{g\mu_l^4}{\sigma_l^3 \rho_l} \tag{12}$$

The Eötvös number, defined as the ratio of gravitational forces to surface tension forces, is given in Eq. (13):

$$Eo = \frac{\rho_l g d_e^2}{\sigma_l} \tag{13}$$

Given the measured bubble diameter and fluid/gas properties of the sodium and argon, it was found that a spherically capped shape was expected for all testing conditions, matching experimental results. The SRT code currently uses Tadaki's correlation to predict bubble eccentricity (Tadaki and Maeda, 1961). Eccentricity can be defined by the aspect ratio of major to minor axis. From this the eccentricity can be found through Eq. (14):

$$E = \begin{matrix} 1 \\ \left(0.81 + 0.206\tanh\left(2(0.8 - log_{10}Ta)\right)\right)^{-3} \\ 4.167 \end{matrix} \quad \begin{matrix} Ta < 1 \\ 1 < Ta < 39.8 \\ Ta > 39.8 \end{matrix} \tag{14}$$

Where Ta is the dimensionless Tadaki number, found through Eq. (15):

$$Ta = Re * M^{0.23} \tag{15}$$

Figure 2 shows a comparison of experimental results to this model. From this, it can be seen that the experimental results follow the model well. The Peebles and Garber correlation is currently used in the SRT code to predict rise velocity. This correlation is split into four segments depending on the shape regime of the bubble being analyzed (Peebles and Garber, 1953). Due to the relatively large size of the bubbles tested, only the correlation for the largest bubble sizes could be tested in a sodium environment. From this, it was found that the correlation greatly under predicted the rise velocity while failing to account for changing bubble size. To account for this, a fifth correlation was added to the model to predict bubble rise velocity for large spherically capped bubbles. This model, presented by Lehrer, is defined according to equation (16) (Lehrer, 1976):

$$V_T = \sqrt{\frac{3\sigma}{d_b\rho_l} + \frac{g d_b \Delta\rho}{2\rho_L}} \tag{16}$$

Figure 3 shows this correlation's fit compared to the experimental data. A complete listing of bubble characteristics can be seen in Table I. Eccentricity is an important metric in bubble scrubbing as it directly influences the surface area to volume ratio of the bubble; more eccentric bubbles experience greater particle scrubbing due to a higher surface area to volume ratio.

A modified approach had to be taken to visualize the bubble swarm testing within the sodium column. Due to the overlapping nature of the bubble swarm flow, individual, distinct bubbles could not be viewed. Instead, only void fraction could be calculated. As bubble size is a crucial parameter of the scrubbing code, initial analysis of the bubble sizes being generated was done in a surrogate water column. Dry air was used as the surrogate gas. The exact injection apparatus was tested to best reflect the planned tests in the sodium pool. Bubbles were imaged using a FASTCAM-Ultima 1024 High-Speed Video Camera and two 500-watt Lowel V-lights provided backlighting. The resulting images had a sharp contrast at the bubble edges. ImageJ was then used to measure the corresponding projected area of each bubble. From the water column bubble sizes, the sizes in a sodium pool with an argon bubble were estimated utilizing the ideal gas law and correlations for flow through a valve. Overall, this correlation found bubbles in the sodium pool, generated under identical conditions, to be five percent larger than those in the water column. These findings were verified experimentally as well by comparing single bubble testing in the water column to that in the sodium column; identical testing conditions were implemented in both the water and sodium columns and the size difference was found to match the correlation. Utilizing the bubble swarm testing in the water column, an average void fraction of 0.379 and a volume weighted average bubble size of 3.66 cm were found for bubble swarm conditions in the sodium pool. Figure 4 shows a representative image of the bubble swarm in the surrogate water column and sodium column.

4. Experimental Apparatus

The testing apparatus used in these experiments was similar to that used in surrogate water column testing (Becker and Anderson , 2021). The testing assembly consisted of three sub-assemblies: the testing column, the aerosol pressure tank, and the collection system. The testing column consisted of an 8-inch, schedule 10, 316 SS pipe. A large diameter pipe was selected such that the drag imposed on the bubbles from the vessel walls would be negligible (Clift *et al.*, 1978). At full volume, 87.0 L of reactor grade sodium were used in the testing. The temperature of the testing section was controlled using LabVIEW and monitored using five thermocouples along the height of the column. The thermocouples were placed 60.1 cm apart with the lowest placed directly at the injection height. The thermocouples were inserted 1.0 cm into the sodium pool so as to be as minimally intrusive as possible and still record accurate temperatures. These thermocouples served to verify the experimental apparatus was isothermal. 1/8 inch, ungrounded, K-type thermocouples with a stated uncertainty of ±2.2 °C were used (Omega, 2022). An additional thermocouple measured the temperature in the cover gas region. The pressure in the cover gas region was monitored using a SITRANS P410 pressure transmitter with 0-30 psi gauge pressure range and uncertainty of ±0.006 psi. Figure 5 shows a 2-D diagram of the testing assembly.

An aerosol pressure tank was utilized to overcome the hydrostatic pressure head present at the injection nozzle. A pressure of 1700 Pa higher than that at the injection nozzle location was held in this vessel. The pressure in the aerosol tank was monitored with the same model pressure transmitter as the cover gas region. A TOPAS SAG 410/U Solid Aerosol Generator was placed within the pressure vessel to aerosolize the surrogate fission product powder into the argon gas flow prior to injection. This device utilized a rotating ring to provide a constant and reproducible amount of powder to the inlet of a venturi suction tube (TOPAS, 2022). As the SRT code is only concerned with the physics of the aerosols and not the chemistry (Bucknor *et al.*, 2017), surrogate aluminum, nickel, and tungsten powders were used to simulate RN aerosols of different density. As the purity of the powders was 99.7%, the particle density was taken to be the element density. The aerosol pressure tank and the testing column were connected through the aerosol injection line. This line consisted of three high temperature solenoid valves. These valves were then actuated in a distinct pattern to maximize the concentration of aerosol being injected; first the dilution flow line was actuated to begin the gas flow. Following this, an inlet valve to the aerosol generator was actuated to replace exiting gas. Once a steady flow had been achieved, the dilution valve was closed at the same time as the outlet valve to the testing column was opened. The outlet valve was then opened for a prescribed time to generate the desired bubble size. All valves were then closed for three seconds to allow the wake in the pool to dissipate prior to the next bubbles injection. The injection line and inlet gas lines were both heated to pool temperature to ensure isothermal conditions between the bubble and coolant pool. Injection gas temperatures were measured directly with a 0.020-inch K-type thermocouple. Losses through each valve were determined experimentally.

After the bubble was allowed to rise through the pool, a dilution cross flow was applied 7.5 cm above the sodium free surface at a flow rate of 15.0 LPM. This flow served to capture the fission products and transport them through the downward facing funnel at the top of the testing column. This funnel reduced the diameter of the testing section to a 1.27 cm diameter tube. The flow then progressed into a coaxial dilution device to further increase the flow rate to 30 LPM. The overall gas flow rate was measured using an Omega FMA6713 flow meter with a 0.3 LPM uncertainty (Omega, 2022). From here, the aerosol entrained flow passes into a MOUDI cascade impactor.

Cascade impactors function by sorting aerosols based on aerodynamic diameter. Particles are sorted into bins by particle size by varying the Stokes number associated with each stage. The Stokes number is defined by Eq. (17):

$$St = \frac{\rho_p C_s V_o D_p^2}{9\mu W} \tag{17}$$

Particles with low Stokes numbers follow streamlines whereas those with large Stokes numbers are dominated by inertia forces and are impacted onto the substrates (Marple *et al.*, 1991). A 10-stage cascade impactor was used with cutoff sizes ranging from 18.0 to 0.056 microns (Marple *et al.*, 1991). A final filter was also used to capture all remaining aerosol following the final stage. Alternating stages were rotated to obtain uniform depositions and maximize collection amounts while minimizing losses. Additionally, each substrate was coated in aerosolized silicon oil to reduce particle bounce. Following coating, each substrate was baked in a furnace at 250°C for 24 hours to eliminate any volatility in their weights. Each substrate was weighed before and after testing to calculate the amounts of aerosols impacted. Each test consisted of 100 sequential, isolate, bubbles to limit uncertainty. Bubble sizes were controlled by solenoid actuation time and were found to be ±20% of the stated value. All measurements were taken on a CPA26P Sartouruis microbalance with a readability of $2\,\mu g$ and a repeatability of $\pm 4\,\mu g$ (Sartourius, 2022). Figure 6 shows a complete setup of the experimental testing apparatus.

5. Testing Methodology

To fully isolate the losses due to bubble scrubbing, a series of six tests needed to be conducted. The six tests were as follows: a calibration test to determine amounts of aerosol being injected, a scrubbing tests to determine DF based on calibration (this test inherently included losses in the system), an injection losses test to quantify aerosol losses upon injection, a collection losses test to determine aerosol losses as they pass through the collection system, sodium vaporization tests to determine amounts and sizes of sodium vapors being produced in the cover gas region with only cross flow, and sodium vaporization tests with bubble flow to determine additional amounts of vaporization due to rising bubbles breaking the free surface. First, due to the high temperature of the sodium pool and vapor pressure of sodium, two sodium vaporization tests were run to quantify the amount of sodium aerosols generated at operating conditions (Makansi *et al.*, 1954). The first set of tests was run with no bubbles passing through the system and only a 15.0 LPM dilution cross flow applied above the pool's free surface. These tests were used to quantify the amounts and sizes of sodium vapor aerosols generated at each pool temperature tested on a per second basis. A second set of tests was run with the same cross flow but with the addition of gaseous argon only bubbles rising through the pool. From these tests, the sodium vaporization amounts due to the cross flow only could be subtracted to isolate the additional amounts of sodium vapor produced due to the bubble flow. While the vaporization due to cross flow was of most importance, the breakage in pool surface due to each rising bubble led to non-negligible amounts of additional sodium vapor.

For the calibration tests, the nozzle outlet was connected directly to the MOUDI impactor. These tests inherently accounted for losses within the collection system and provided a baseline from which to calculate the overall DF. The amounts of particles injected were quantified on a mass basis. An additional set of tests was conducted to measure the amounts of aerosols scrubbed throughout the entire system. To perform these tests, the testing apparatus was setup as described

in the experimental apparatus section of this paper. The aerosol generator was operated at the exact settings used in the calibration tests. The amounts of aerosols collected in the MOUDI impactor were then measured. However, these tests alone did not directly reflect the amount of scrubbing due to bubble transport since additional sources of losses were present; losses upon injection and losses in the collection system were present in this measurement. As the aerosol must pass through the collection system prior to being categorized by size, these losses are inherently in this overall measurement. Further, as a downward facing nozzle is used to produce the bubbles, there are additional losses as the bubble quickly changes direction due to the buoyancy force acting on the bubble.

To determine these losses, two additional sets of experiments were conducted to isolate all methods of particle losses. The first set was conducted with the injection nozzle placed upward, directly at the would be free surface of the sodium pool in an empty vessel. The aerosol generator was then run with normal operating conditions and the amounts of aerosols collected on the impaction plate were used to find the ratios of aerosols lost in the collection system. The percentage of losses in the collection system were defined as the ratio of the collection loss test to the calibration tests. These losses were largely minimal for particle sizes ranging from 0.01 to 1 micron in size with losses of less than three percent. However, for particle sizes between 1.8 and 3.2 microns, losses of up to 10 percent were seen. For the largest particle sizes tested, losses varied from 15 to 25 percent. A final set of experiments was conducted with the nozzle placed downward just below the free surface of the sodium pool. With minimal residency time within the pool for the aerosol entrained bubbles, all losses were due to injection. From these tests, the percent of losses due to injection were calculated and the overall DF was adjusted accordingly. Experimentally, these losses were found to account for between 10 and 50 percent of the overall scrubbing amounts. The percentage of losses varied by particle size and, generally, higher losses were seen for larger particle sizes.

From these six tests, the overall DF could be determined. The DF is defined according to Equation (18):

$$DF = \frac{Aerosol\ mass\ enter\ the\ sodium\ pool}{Aerosol\ mass\ exiting\ the\ sodium\ pool} \tag{18}$$

The six tests are combined to find the overall DF according to Equation (19):

$$DF = \frac{Cal * IL}{\frac{Scr}{CL} - \left(SV_{crossflow} * time + SV_{bubble} * \#bubbles\right)} \tag{19}$$

Where Cal is the calibration tests, IL is the percent of losses due to injection, Scr is the scrubbing tests, CL is the percent of losses due to transport through the collection system, $SV_{crossflow}$ is the sodium vaporization due to cross flow only, and SV_{bubble} is the sodium vaporization due to bubble flow only. Percent losses were calculated for each particle size bin and are defined by the ratio of particle exiting a subsystem to those entering.

A sensitivity study of the SRT bubble code was performed to determine the variables of key interest. From this study, particle size, bubble size, pool temperature, pool depth, and aerosol density were all found to have significant impacts on the overall DF. Aerosol concentration was found to have no effect on the overall DF, however due to findings in past literature it too was

included (Miyahara *et al.*, 1996). As a result, each of these variables were isolated and varied to assess their importance experimentally. In total eleven sets of tests were conducted. A complete testing matrix can be seen in Table II. In this table, aerosol concentration is defined as the mass of aerosols inside the bubble to the volume of the bubble. Particle density is the elemental density of the aerosol powder. The number of aerosols in each bin sizes was found by dividing the total mass for the respective bin size by the particle density and the average volume for the respective bin size. Particle number density was then found by dividing the number of aerosols in each bin size by the volume of the bubble. For each of these sets, six tests were needed for each variation of a key parameter. In addition, each of these tests were repeated five times to reduce uncertainties and analyze reproducibility of the results. A final set of tests was run with a sparging device to generate a bubble swarm to analyze the effects of more prototypic conditions. The sparging device was a linear tube with seven 1.016 mm holes drilled at varying radial positions along the length of the device. A flow rate of 15.0 LPM was utilized for the bubble swarm tests. In total 360 tests were conducted.

6. Results

Prior to analyzing bubble scrubbing trends, a thorough understanding of sodium vaporization from the pool was required. With cross flow only across the pool free surface, significant sodium vaporization occurs. As these aerosols also deposit within the MOUDI impactor, quantifying them was required. Figure 7 displays the amount of sodium vapor collected for the various pool temperatures tested. In this figure, each temperature was tested at a pool depth of 1.822 m aside from the data points explicitly stating otherwise. As can be seen, vaporization amounts increase exponentially with pool temperature; at 150.°C, the vaporization amounts are negligible compared to the powder aerosol quantities, but at 300.°C, they are the dominant mass collected on the substrates for certain sizes. As temperatures increased, the mean size of sodium vapor aerosols changed as well. This is likely due to sodium vapor aerosols agglomerating in larger quantities due to the greater concentration of them at higher temperatures. With design temperatures in the reactor core of 550.°C, sodium vaporization from the pool is expected to produce a significant portion of aerosols in the cover gas region.

Further testing was done to study the effects of bubbles on sodium vaporization. Successive rising bubbles breaking the free pool surface repeatedly were found to produce greater amounts of vaporization. Figure 8 shows experimental data for various bubble sizes at a pool temperature of 200.°C. The vaporization amounts are given on a mass per second basis, but an inclusion of vaporization due to 100 bubbles is included to better illustrate the effects of bubbles. As can be seen, the introduction of bubbles breaking the pool surface increases sodium vaporization amounts. However, comparing the additional amount of vaporization, on a per 100 bubble basis, to that from cross flow only, on a per second basis, it is apparent that the additional vaporization due to each bubble is minimal, although not negligible. The sodium vapor sizes due to bubble flow are significantly greater than those for cross flow only and thus must be accounted for to accurately determine the overall DF.

With sodium vapor aerosols understood, a series of tests was conducted to focus on various key parameters affecting the overall DF. Bubble size was found to have a key effect on bubble scrubbing for several reasons. Examining Eqs. 1-10, it can be seen that increasing bubble size directly reduces the scrubbing rates of Brownian diffusion, inertial deposition, and gravitational sedimentation. However, bubble size also directly influences bubble rise velocity and

eccentricity. Combined, larger bubbles tend to have lower overall scrubbing for all particle sizes. This is most evident for particle sizes greater than 1.0 micron and less than 0.1 micron. Figure 9 shows the experimental results compared to the SRT model. In this figure, the square dots represent data points, the solid lines connect data points for easier visualization, and the dashed lines represent the SRT model. The experimental results had larger DF than was predicted by the SRT model, suggesting the SRT model represents a conservative estimate of the overall bubble scrubbing. This conservatism can largely be explained by simplifications made within the model, however the penetration theory used for Brownian diffusion is non-conservative in nature. This could be explained by particle growth due to vapor condensation. Sun *et al.* has demonstrated that growth due to vapor condensation can significantly impact the overall DF (2021). However, this is not likely in sodium due to its relatively high surface tension; less than four percent changes in particle diameter are expected for the aerosol sizes tested based on correlation from Sun *et al.* (2021). Additionally, particle agglomeration during the bubble rise may have artificially increased the DF values for small particle sizes. Large uncertainties make it difficult to examine trends in the ranges of 0.056 to 1.0 micron, however trends are followed within the margins of error. At the extreme particle sizes tested, the cut off sizes, or sizes where appreciable scrubbing occurs, match for the experimental and theoretical results. This provides better insights on what particles sizes are of concern.

The results for varying pool temperatures had negligible differences over the temperatures tested. As the setup was isothermal, pool and bubble temperatures were equalized. Only Brownian diffusion is a function of bubble temperatures, increasing proportional to the square root of bubble temperature. Being the dominant mode of scrubbing for relatively small particle sizes, an increase in DF for small particle sizes was expected. However, as pool temperature increased, bubble size also increased despite identical bubble generation conditions. This was due to a slight increase in flow through the solenoid valves at higher temperatures. As previously shown, increasing bubble size results in decreased scrubbing. The influence of increased pool temperature compared to increased bubble size are similar in magnitude and thus essentially negate one another. Changes in bubble size also effect scrubbing for larger aerosols sizes, however to a minimal extent due to only small changes in bubble size. Overall, it is hard to draw conclusions for the experimental data due to negligible changes in scrubbing amounts. However, as shown in Figure 10, the experimental data reflect the SRT predictions are within the margins of uncertainty and follows a similar trend with respect the DF as a function of aerosol sizes.

A series of tests was conducted at varying pool heights with identical aerosol and bubble conditions to study the isolated effects of pool depth on scrubbing. Intuitively, greater pool depth results in more scrubbing due to an increased bubble residence time. This can be seen in the overall DF equation as each rate constant is multiplied by the pool depth to obtain the overall DF. This trend was also matched experimentally where marked differences are observed. Again, the trends are harder to visualize in particle sizes between 0.056 and 1.0 micron due to experimental uncertainty. However, Figure 11 shows the general trends are closely matched. Due to the large lengths of fuel rods, the location of breach has great significance on the amounts of RN scrubbed.

As a large variety of fission products are created during typical reactor operating conditions, tests were run to isolate the effects of aerosol density on the DF. Simulations in the SRT scrubbing model found Brownian diffusion to have no dependance on aerosol density. Gravitational sedimentation and inertial deposition both increased proportional to increasing aerosol density.

Due to this, small particle sizes, where Brownian diffusion is dominant, are largely unaffected by changing aerosol density while relatively large particle sizes vary considerably. Figure 12 displays this trend. Comparing this to the experimental results, it can be seen that a similar trend is found; larger particle sizes are found to have considerable difference in scrubbing amounts while smaller particle sizes all have similar scrubbing amounts.

Sensitivity analyses in the SRT bubble scrubbing code found DF to be independent of aerosol concentrations. Past literature, however, had found aerosol concentration to be a key factor in the overall DF (Miyahara, 1996; Sun 2019). As a result, an additional series of tests was conducted to analyze its effects. Figure 13 shows the experimental results compared to the SRT model. While there are slight deviations in the experimental values, these are all within in the margins of uncertainty. Overall, the experimental results follow the trends of the SRT model well with no appreciable changes in DF.

The majority of testing was conducted using a single isolated bubble to best reflect the SRT bubble scrubbing code. This model, however, fails to accurately represent the predicted flow regime in the event of a postulated fuel pin failure. To better reflect this, a sparging device was used to create a heterogenous bubble swarm. A volumetric weighted mean average was used to characterize the bubble size in the SRT code. The results were also compared to results from the similarly sized 3.632 cm bubble tests to compare between the single isolated bubble and the bubble swarm conditions. Figure 14 shows a plot of the results. The results of the bubble swarm testing match the trends from both the SRT code and the single isolated bubble well. However, considerably more scrubbing was found for the bubble swarm testing for all particle sizes. This is likely due to the turbulent nature of the flow; considerable bubble breakup, agglomeration, and mixing was observed. In a fuel pin failure, due to the high pressures anticipated (Bucknor *et al.*, 2017), scrubbing conditions similar to the bubble swarm testing are expected. Additionally, the tight geometry between fuel pins would result in impingement of bubbles on fuel pin wire wrap, likely resulting in further scrubbing. From this, it is found that the SRT scrubbing code presents a conservative estimate of the total amounts of scrubbing found experimentally; a 4x increasing in scrubbing is found in the experimental results compared to the model.

7. Uncertainty

All uncertainties stated are within a 95% confidence interval and utilize a single-sample uncertainty method (Moffat, 1988). Uncertainty was calculated by combining the uncertainty in each of the six tests utilized. Uncertainty values varied considerably with aerosol size and by type of test conducted. All uncertainty values were found to be within $\pm 30\%$ of the stated value. Generally, uncertainty amounts were highest for particle sizes greater than 3.2 microns due to the large amounts of aerosol scrubbing in this range. Particle sizes between 0.32 and 1.0 micron had uncertainties less than $\pm 20\%$ of the stated value. Aerosol sizes less than 0.18 microns had uncertainties less than $\pm 25\%$ of the stated value. Exceptions to this are aerosol sized near 1 micron for tests with pool temperatures of 300.°C due to large amounts of sodium vapor. 0.18-micron aerosol size also had larger uncertainties at temperature of 200.°C and 300.°C due to large amounts of sodium vapor aerosols at this size under these conditions.

8. Conclusion

This work was successful in validating the SRT scrubbing code along with several key correlations within it. The current bubble rise velocity correlation found within the SRT code was found to not accurately predict rise velocities for spherically capped bubbles. Due to this the Lehrer correlation was added for bubbles in the spherically capped shape regime. This correlation was found to closely match the experimental results. Additionally, Tadaki's correlation was validated in a sodium pool environment. Furthermore, sodium vaporization from the pool's free surface was quantified for various temperatures with a 15.0 LPM cross flow. From this it was found that sodium vaporization amounts increase exponentially with temperature.

Several key findings were also made in regard to bubble scrubbing. The effects of bubble size, pool temperature, pool depth, aerosol density, and aerosol concentration on bubble scrubbing were analyzed over a wide range of aerosol sizes. Increasing bubble size was found to decrease overall scrubbing for all particle sizes. Pool temperature was found to have little effect on the overall scrubbing amounts due to an offsetting of increased scrubbing due to pool temperature by decreased scrubbing due to increased bubble size. Decreased pool depth was found to decrease scrubbing for all particle sizes due to a decrease in bubble residence time. Increased aerosol density was found to greatly increase scrubbing for relatively large aerosol sizes (i.e. greater than 0.1 micron), but have negligible impact on smaller particle sizes. Lastly, varying aerosol concentration was found to have negligible impact on scrubbing for all particle sizes. Comparing to the SRT scrubbing model, the experimental results matched the general trends predicted by the model. However, the model predicts a conservative estimate for the overall DF when compared to the experimental results. This is largely due to simplifications in the code such as not accounting for complex hydrodynamic phenomena and additional scrubbing mechanisms. Past literature has shown limitation in Fuchs model, as described previously in this paper, and additional research is needed to develop a more realistic model. A final test was conducted to analyze the effects of a bubble swarm compared to the single isolated bubble model. From this, it was found that significantly more scrubbing is found in a heterogenous bubbly flow regime than in the single isolated bubble case, further widening the gap between the model and the experimental results. Despite this, the trends in DF as a function of aerosol size were matched in all case.

A series of future tests would be useful to analyze the effects of a fuel pin assembly on bubble scrubbing. As has been shown in this research, bubble to bubble interactions have a significant impact on the DF. The additional geometric constraints of a prototypic SFR fuel pin assembly is theorized to further increase scrubbing amounts and efforts to quantify this increase would be invaluable to SFR licensing.

Acknowledgements

This work was funded in part by the Department of Energy Office of Nuclear Energy's Nuclear Energy University Program under Award Number DE-NE0008804 along with support from the University of Wisconsin-Madison Thermal Hydraulics Laboratory. The views and opinions of authors expressed herein do not necessarily state or reflect those of the United States Government or any agency thereof.

Data Availability

Raw data regarding bubble scrubbing can be found at DOI: 10.17632/7cgrcc3xd5.1 (Becker, 2022).

Bibliography

Becker, K., 2022. Data for: Experimental Validation of Simplified Radionuclide Transport Bubble Scrubbing Code in Sodium Coolant Pool. Mendeley Data, V1, https://doi.org/10.17632/7cgrcc3xd5.1

Becker, K., Anderson, M., 2021. Experimental study of SRT scrubbing model in water coolant pool. Nucl. Eng. Des., vol. 307. https://doi.org/10.1016/j.nucengdes.2021.111130

Bucknor, M., Farmer, M.T., Grabaskas, D., 2017. An Assessment of Fission Product Scrubbing in Sodium Pools Following a Core Damage Event in a Sodium Cooled Fast Reactor. International Conference on Fast Reactors and Related Fuel Cycles: Next Generation Nuclear Systems for Sustainable Development (FR 17), Yekaterinburg, RU.

Clift, R., Grace, J.R., Webber, M.E., 1978. Bubbles, Drops, and Particles. Academic Press, New York (NY).

Dehbi, A., Suckow, D., Guentay, S., 2001. Aerosol retention in low-subcooling pools under realistic accident conditions. Nucl. Eng. Des., vol 203, no. 2-3, pp. 229-241. https://doi.org/10.1016/S0029-5493(00)00343-5

"GE Optima XR220," GE. Accessed May 29, 2022, from https://www.gehealthcare.com/products/radiography/mobile-xray-systems/optima-xr220amx

Grabaskas, D., Brunett, A.J., Bucknor, M., Sienicki, J., and Sofu, T., 2015. Regulatory Technology Development Plan - Sodium Fast Reactor: Mechanistic Source Term Development. Argonne National Laboratory ANL-ART-3. https://doi.org/10.2172/1179443

Grabaskas, D., Bucknor, M., Jerden, J., 2016. Regulatory Technology Development Plan - Sodium Fast Reactor: Mechanistic Source Term Development – Metal Fuel Radionuclide Release. Argonne National Laboratory, ANL-ART-38. https://doi.org/10.2172/1245176

Grabaskas, D., Bucknor, M., Jerden, J., Brunett, A.J., Denman, M., Clark, A., et al., 2016. Regulatory Technology Development Plan - Sodium Fast Reactor: Mechanistic Source Term Development – Trial Calculation. Argonne National Laboratory, ANL-ART-49. https://doi.org/10.2172/1334189

Hakii, J., Kaneko, I., 1990. Experimental study on aerosol removal efficiency for pool scrubbing under high temperature steam atmosphere. Proceedings of 21st DOE/NRC Nuclear Air Cleaning Conference, San Diego, 13-16th.

Flanagan, G., Fanning, T., Sofu, T., 2005. Sodium-cooled Fast Reactor (SFR) Technology and Safety Overview. Presented at Office of Nuclear Energy, US DOE, Washington DC, February 18.

Flanagan, G., Fanning, T., Sofu, T., 2015. Sodium-cooled Faster Reactor (SFR) Technology Overview. IAEA Education and Training Seminar on Fast Reactor Science and Technology, Santa Fe, NM.

Fuchs, N.A., 1964. The Mechanics of Aerosols. Pergamon Press, New York, NY.

Kanai, T., Furuya, M., Arai T., Nishi, Y., 2016. Development of an aerosol decontamination factor evaluation method using an aerosol spectrometer. Nucl. Eng. Des., vol. 303, pp. 58- 67. https://doi.org/10.1016/j.nucengdes.2016.04.011

Kaneko, I., Fukasawa, M., Naito, M., Miyata, K., Matsumoto, M., 1992. Experimental study on aerosol removal effect by pool scrubbing. 22nd DOE/NRC Nuclear Air Cleaning and Treatment Conference.

Lehrer, H.G.A, 1976. A rational terminal velocity equation for bubbles and drops at intermediate and high Reynolds numbers. J. Chem. Eng. Jpn., pp. 237, vol. 9. https://doi.org/10.1252/jcej.9.237

Li, Y., Ma, Q., Sun, Z., Gu, H., Zhou, Y., and Shi, K., 2019. Study on calculation method of soluble aerosol removal efficiency under high humidity conditions. Front. in Energy Res., vol.7. https://doi.org/10.3389/fenrg.2019.00026

Liu, J., He, Y., 2019. Heat-transfer characteristics of liquid sodium in a solar receiver tube with a nonuniform heat flux. Energies, vol. 12. no. 8. https://doi.org/10.3390/en12081432

Makansi, M.M., Madsen, M., Selke, W.A., 1954. Determination of the vapor pressure of sodium. J. Phys. Chem. vol. 59, pp. 40-42.

Marple, V.A., Rubow, K.L., Behm, S.M., 1991. A microorifice uniform deposit impactor (MOUDI): Description, calibration, and use. Aerosol Sci. Technol., vol. 14, no. 4, pp. 434-466. https://doi.org/10.1080/02786829108959504

Mills, A.F., Hoseyni, M.S., 1988. Diffusive Deposition of Aerosols in a Rising Bubble. Aerosol Sci. Technol., pp 103-105, vol 8. https://doi.org/10.1080/02786828808959174

Miyahara, S., Norihiko S., Kazuhito S., 1996. Iodine mass transfer from Xenon-Iodine mixed gas bubble to liquid sodium pool. J. Nucl. Sci. Technol., pp. 128-133, vol. 33, no. 2. https://doi.org/10.1080/18811248.1996.9731874

Moffat, R.J., 1988. Describing the uncertainties in experimental results. Exp. Therm. Fluid Sci., vol. 1, pp. 3–17. https://doi.org/10.1016/0894-1777(88)90043-X

Motegi, K., Sibamoto, Y., Kukita, Y., 2022. Nonuniform particle distribution and interference between removal mechanisms during unsteady aerosol deposition from a rising spherical bubble. J. Nucl. Sci. Tehnolo., pp. 1037-1046, vol. 59, no. 8. https://doi.org/10.1080/00223131.2022.2029724

"Omega Thermocouple Types," Omega, Accessed, May 29, 2022. [Online]. Available: from https://www.omega.com/en-us/thermocouple-types

"Omega Multi Parameter Mass Flowmeter," Omega, Accessed, May 29, 2022, [Online]. Available: https://cn.omega.com/pptst_eng/FMA6600_FMA6700.html

Peebles, F. N., Garber, H. J., 1953. Studies on the motion of gas bubbles in liquid. Chem. Eng. Progr., pp. 88-97, vol. 49, no. 2.

Powers, D.A., Sprung, J.L., 1993. A Simplified Model of Aerosol Scrubbing by a Water pool Overlying Core Debris Interacting with Concrete. NUREG/CR-5901.

Pradeep A, Sharma A. K., 2018. Semiempirical model for wet scrubbing of bubble rising in liquid pool of sodium-cooled fast reactor. Nucl. Eng. Technol., pp. 849-853, vol. 50. https://doi.org/10.1016/j.net.2018.04.003

"SAG 410 – Dosing Range 0.5mg/h up to 6kg/h," TOPAS, Accessed: July 7, 2020. [Online]. Available: https://www.topas-gmbh.de/en/produkte/sag-410/

"Sartorius CPA26P Microbalance," Sartorius, Accessed July 9, 2020. [Online]. Available: https://scaleman.com/micro-balance-weighing-sartorius-cpa26p.html

Sun, H., Sibamoto, Y., Okagaki, Y., Yonomoto, Y., 2019. Experimental Investigation of Decontamination Factor Dependence on Aerosol Concentration in Pool Scrubbing. Sci. Technol. Nucl., vol. 2019. https://doi.org/10.1155/2019/1743982

Sun, H., Sibamoto, Y., Hirose, Y., Kukita, Y., 2021. The dependence of pool scrubbing decontamination factor on particle number density: modeling based on bubble mass and energy balances. J. Nucl. Sci. Technol., pp. 1048-1057, vol. 58, no. 9. https://doi.org/10.1080/00223131.2021.1907254

Tadaki, T., Maeda, S., 1961. On the shape and velocity of single air bubbles rising in various liquids. Kagaku Kogaku, vol. 25, pp. 254-264.

Thormeier, K., 1970. Solubility of the Noble Gases in Liquid Sodium. Nucl. Eng. Des., vol. 14, no. 1, pp. 69-82. https://doi.org/10.1016/0029-5493(70)90085-3

Wassel, A.T., Mills, A.F., Bugby, D.C., 1985. Analysis of Radionuclide Retention in Water Pools. Nucl. Eng. Des. vol. 90. https://doi.org/10.1016/0029-5493(85)90033-0

Yoshida, K., Fujiwara, K., 2021. Experimental study on bubble and aerosol behavior during pool scrubbing. 28th International Conference on Nuclear Engineering, ICONE28-61490. https://doi.org/10.1115/ICONE28-61490

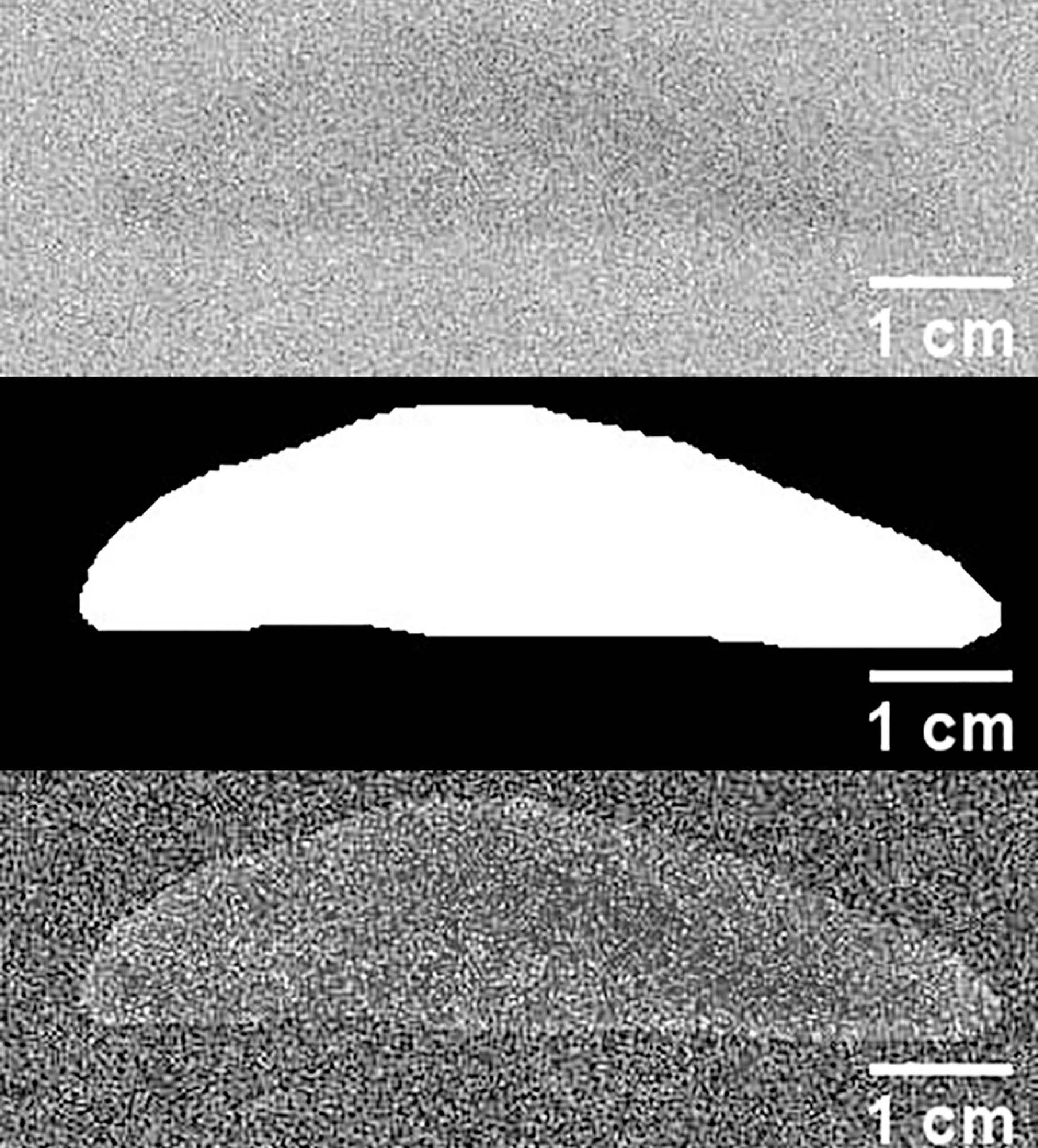
1 cm
1 cm
1 cm

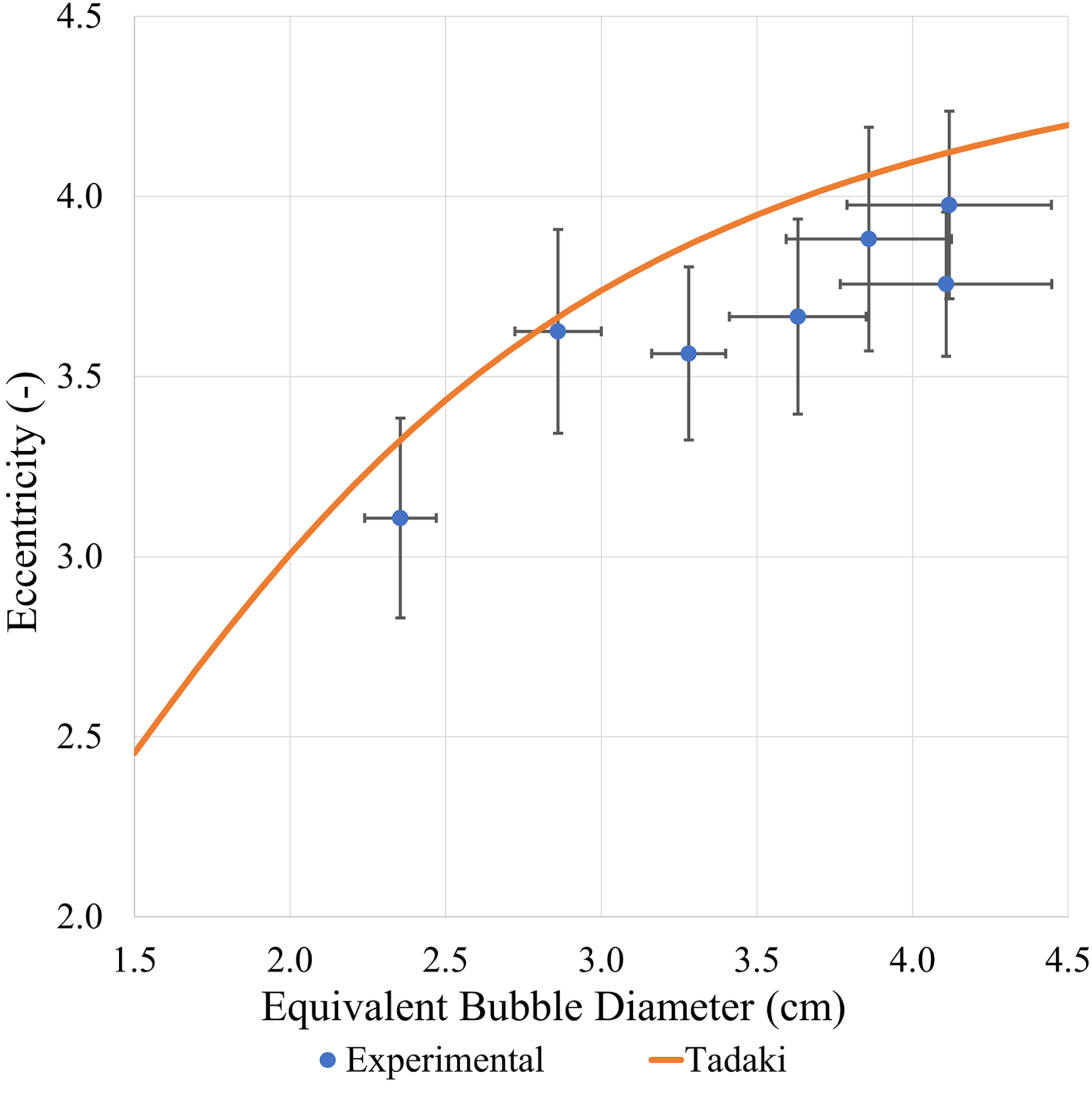
4.5
4.0
3.5
3.0
2.5
2.0
Eccentricity (-)
1.5
2.0
2.5
3.0
3.5
4.0
4.5
Equivalent Bubble Diameter (cm)
Experimental
Tadaki

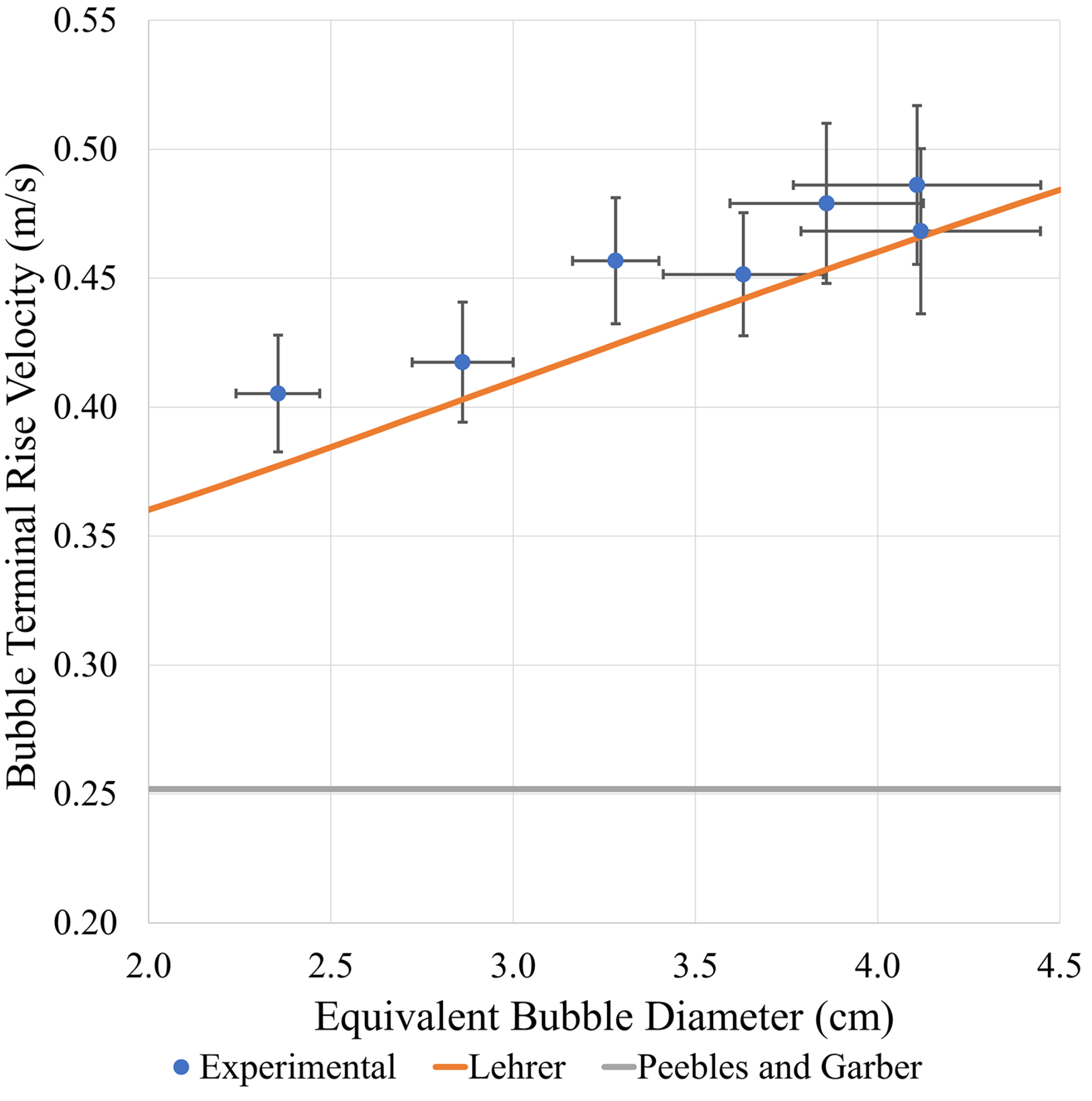
0.55
0.50
0.45
0.40
0.35
0.30
0.25
0.20
Bubble Terminal Rise Velocity (m/s)
2.0
2.5
3.0
3.5
4.0
4.5
Equivalent Bubble Diameter (cm)
Experimental
Lehrer
Peebles and Garber

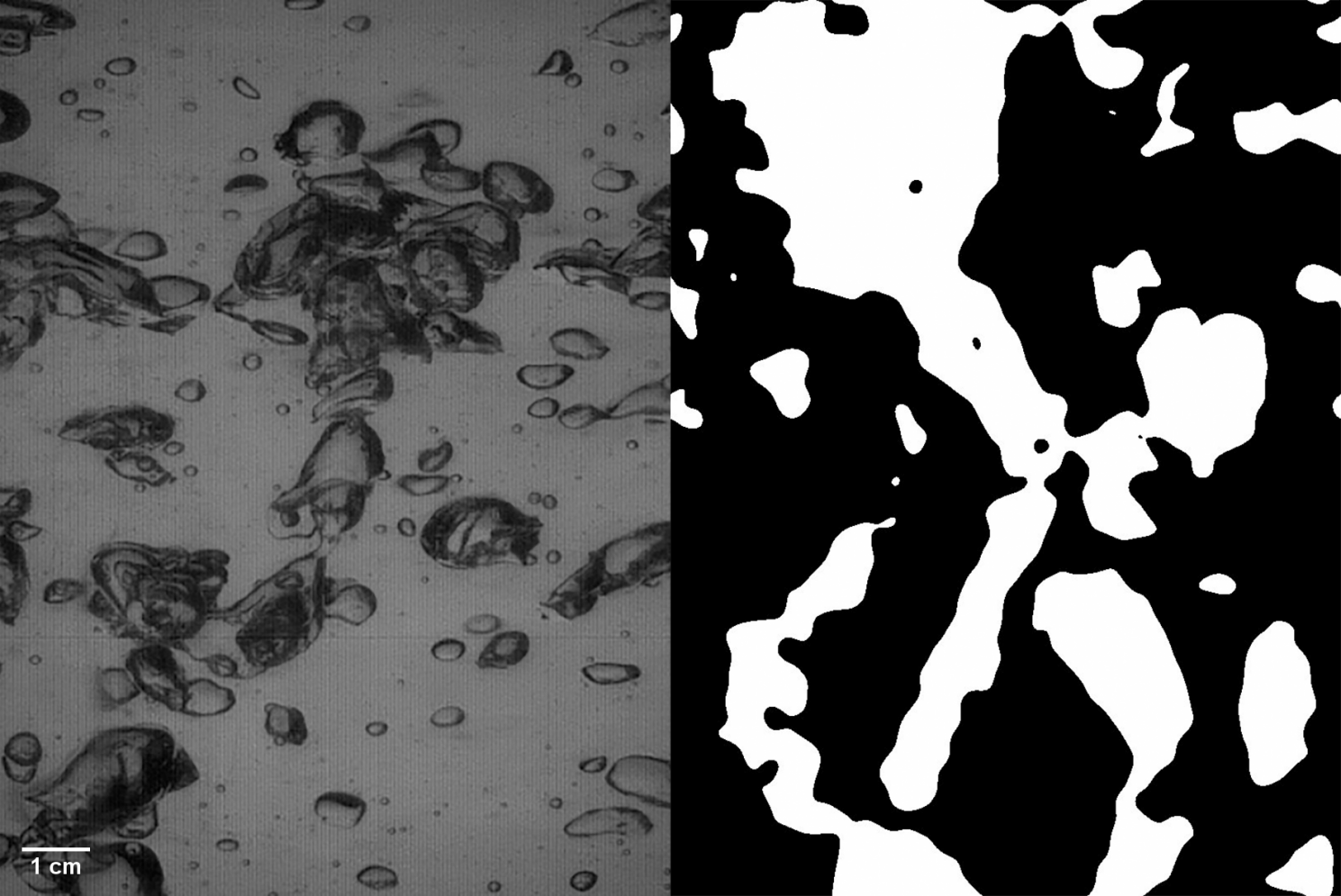
1 cm

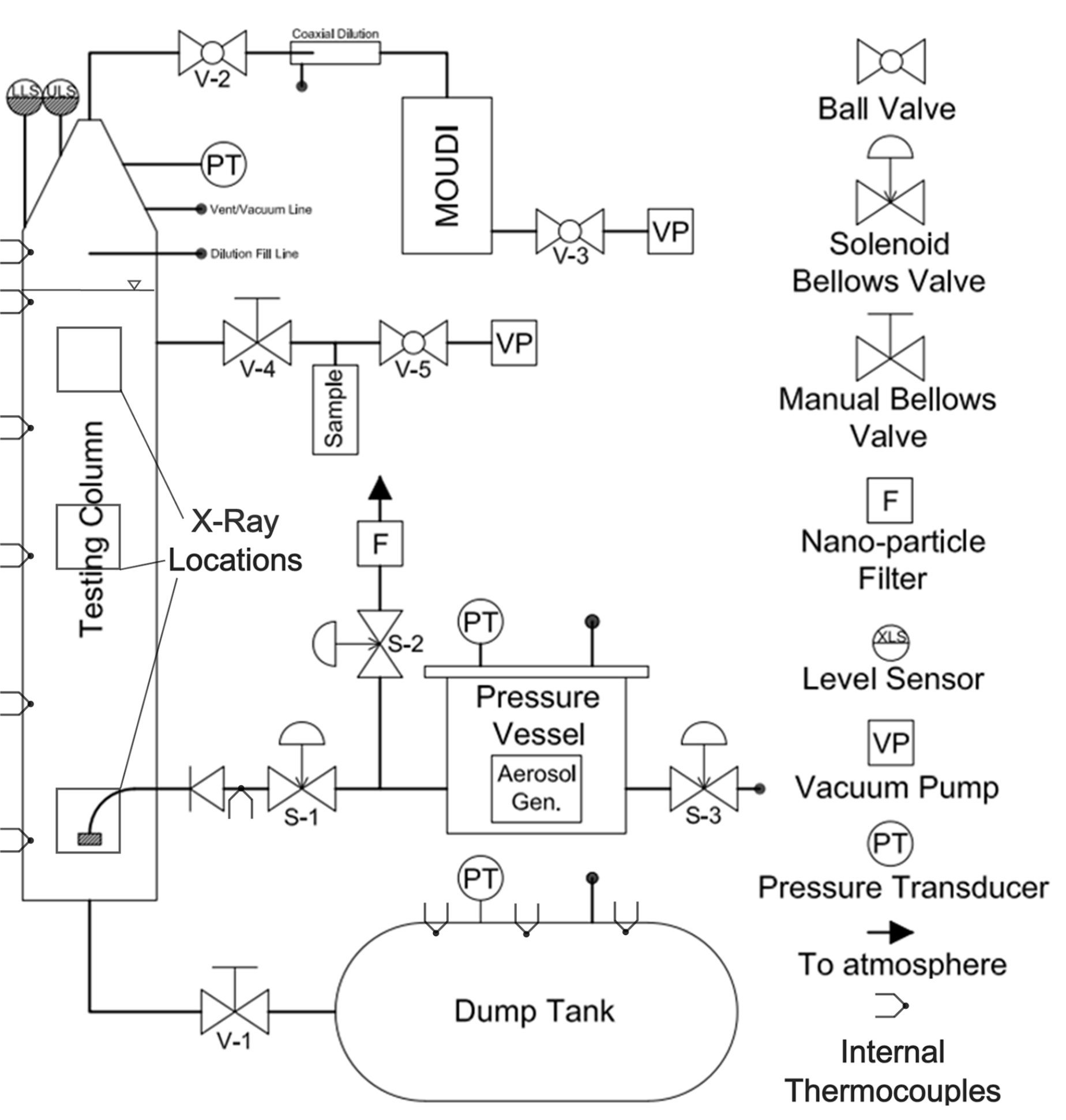
Coaxial Dilution
V-2
LLS
ULS
PT
Vent/Vacuum Line
Dilution Fill Line
MOUDI
V-3
VP
V-4
Sample
V-5
VP
Testing Column
X-Ray Locations
F
S-2
PT
Pressure Vessel
Aerosol Gen.
S-1
S-3
PT
Dump Tank
V-1
Ball Valve
Solenoid Bellows Valve
Manual Bellows Valve
F
Nano-particle Filter
XLS
Level Sensor
VP
Vacuum Pump
PT
Pressure Transducer
To atmosphere
Internal Thermocouples

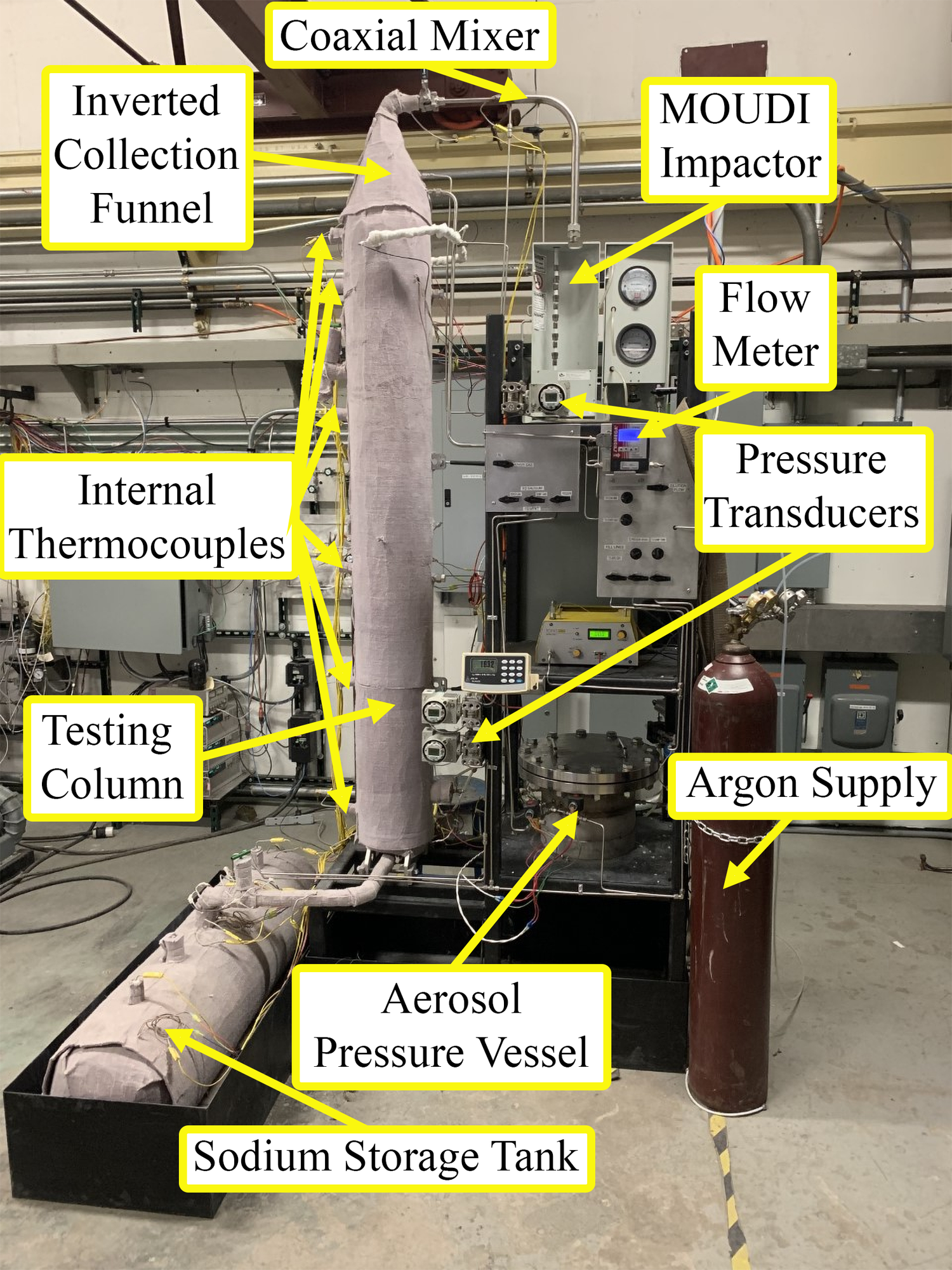
Coaxial Mixer
Inverted Collection Funnel
MOUDI Impactor
Flow Meter
Pressure Transducers
Internal Thermocouples
Testing Column
Argon Supply
Aerosol Pressure Vessel
Sodium Storage Tank

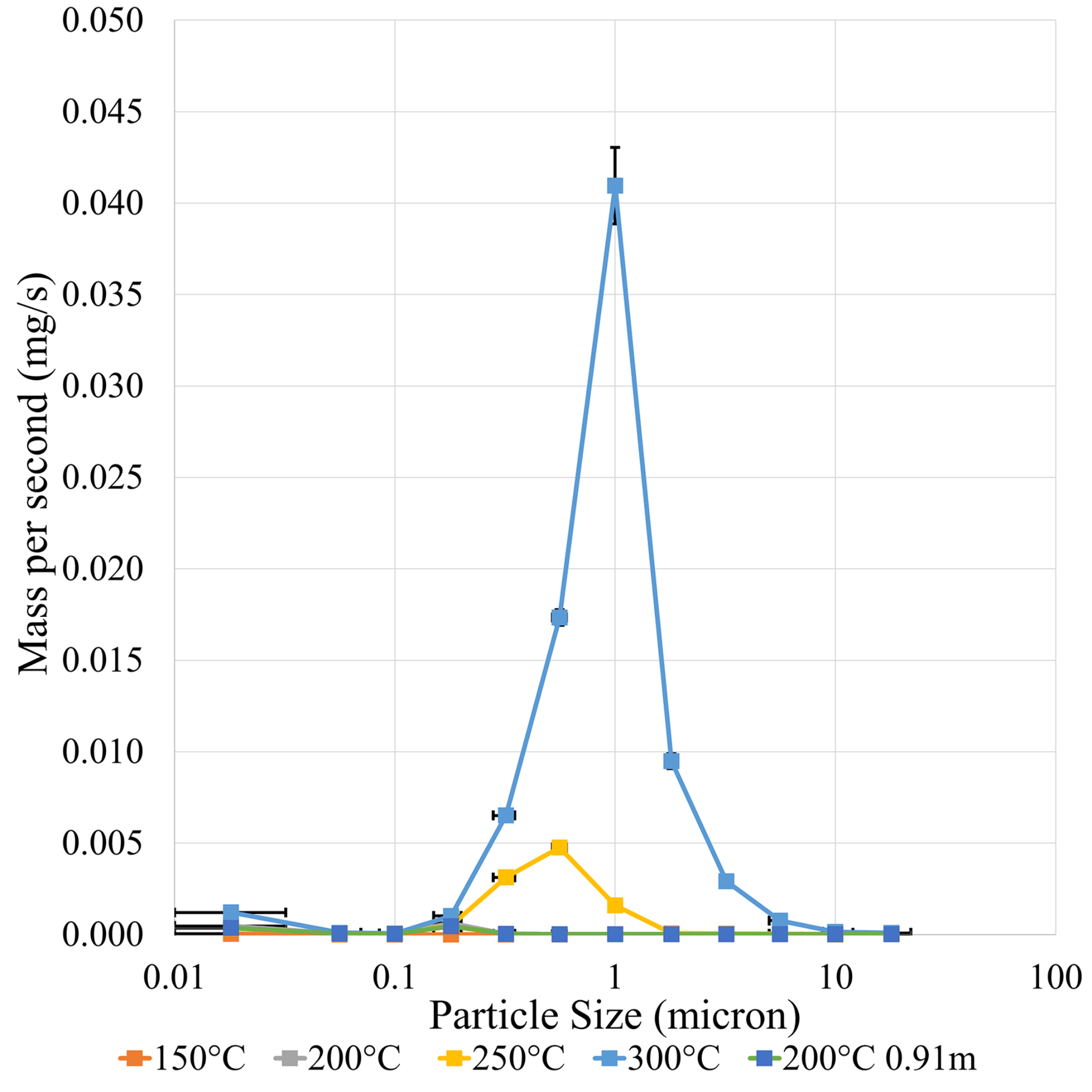
0.050
0.045
0.040
0.035
0.030
0.025
0.020
0.015
0.010
0.005
0.000
Mass per second (mg/s)
0.01
0.1
1
10
100
Particle Size (micron)
150°C
200°C
250°C
300°C
200°C 0.91m

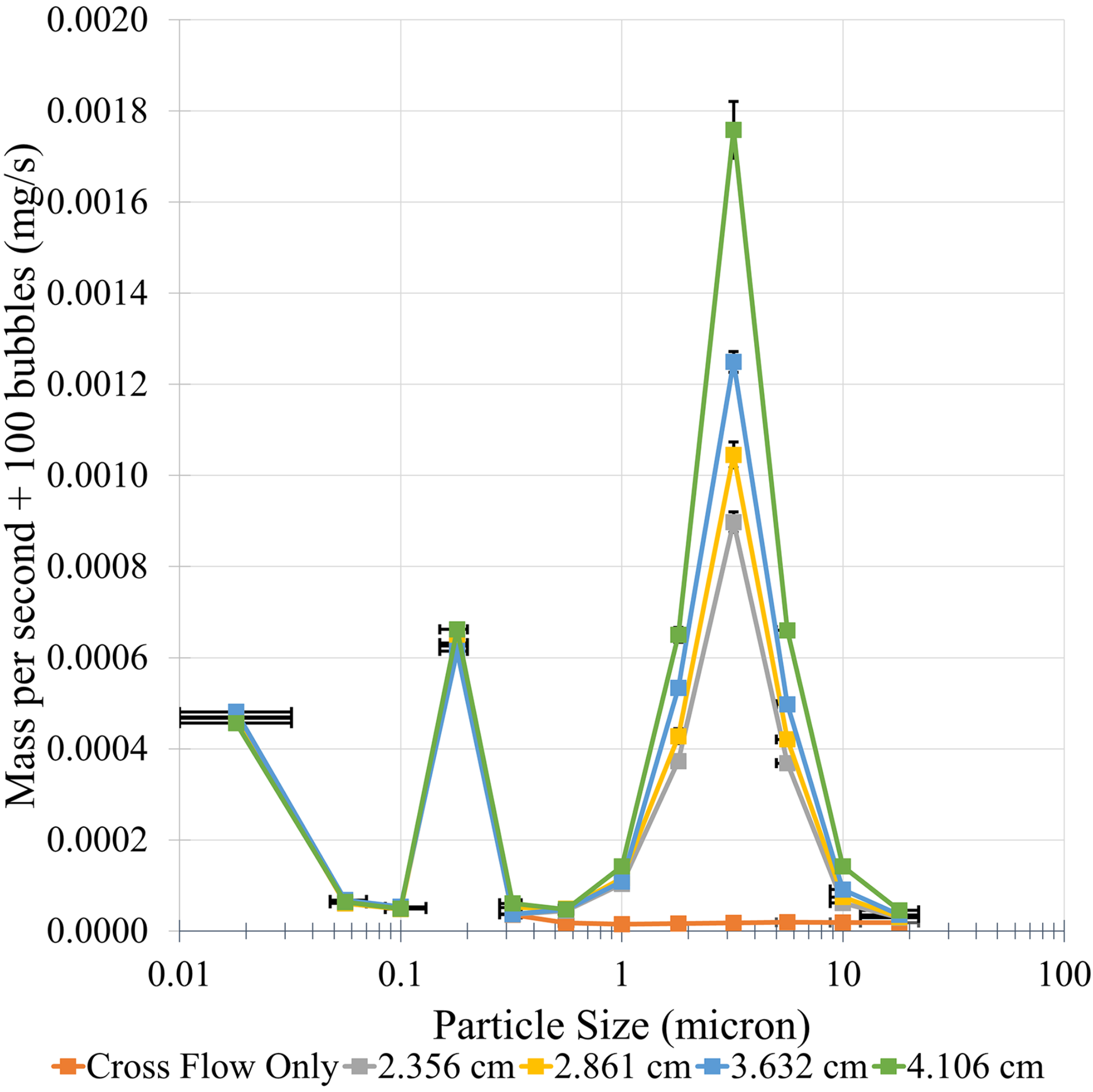
0.0020
0.0018
0.0016
0.0014
0.0012
0.0010
0.0008
0.0006
0.0004
0.0002
0.0000
Mass per second + 100 bubbles (mg/s)
0.01
0.1
1
10
100
Particle Size (micron)
Cross Flow Only
2.356 cm
2.861 cm
3.632 cm
4.106 cm

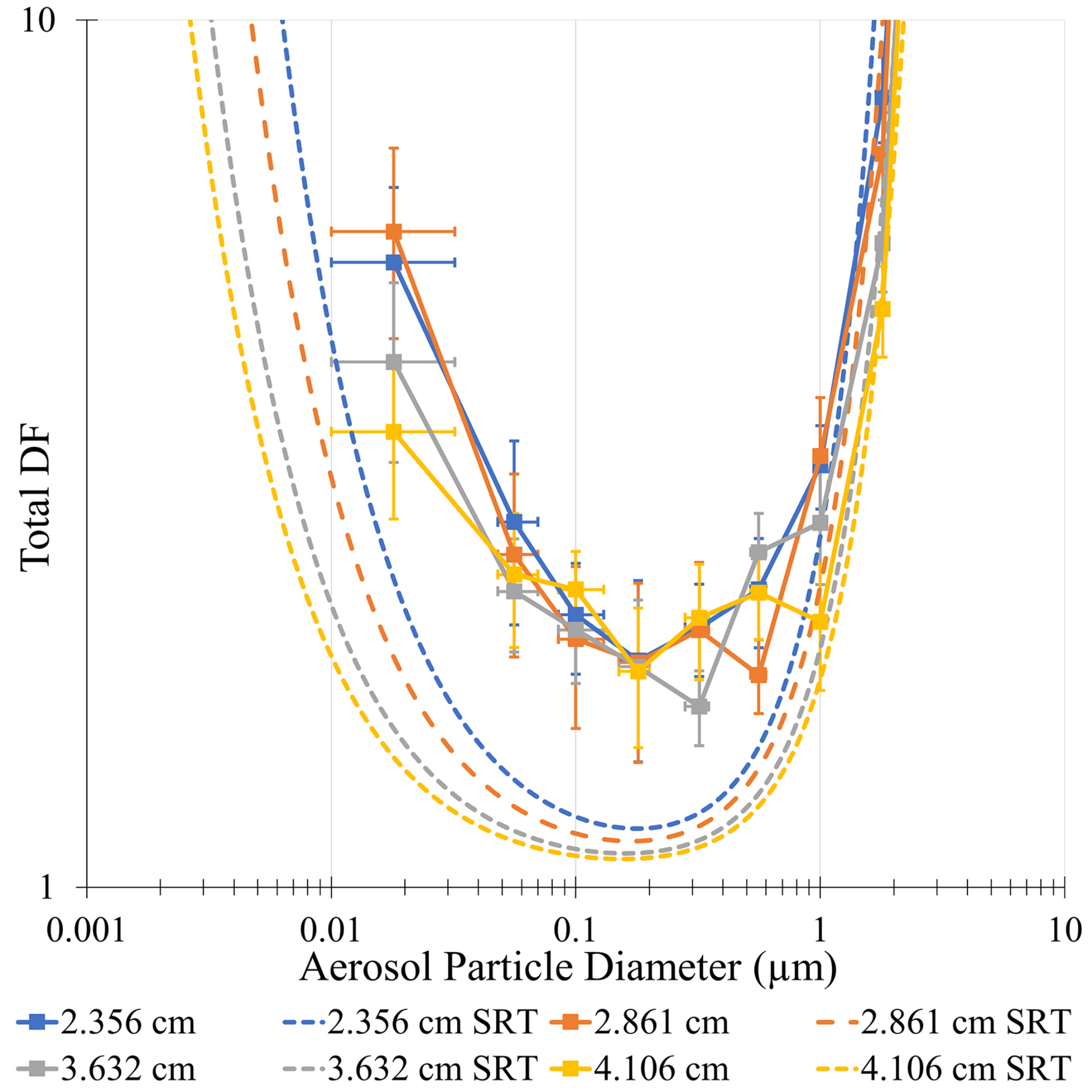
10
1
Total DF
0.001
0.01
0.1
1
10
Aerosol Particle Diameter (µm)
2.356 cm
2.356 cm SRT
2.861 cm
2.861 cm SRT
3.632 cm
3.632 cm SRT
4.106 cm
4.106 cm SRT

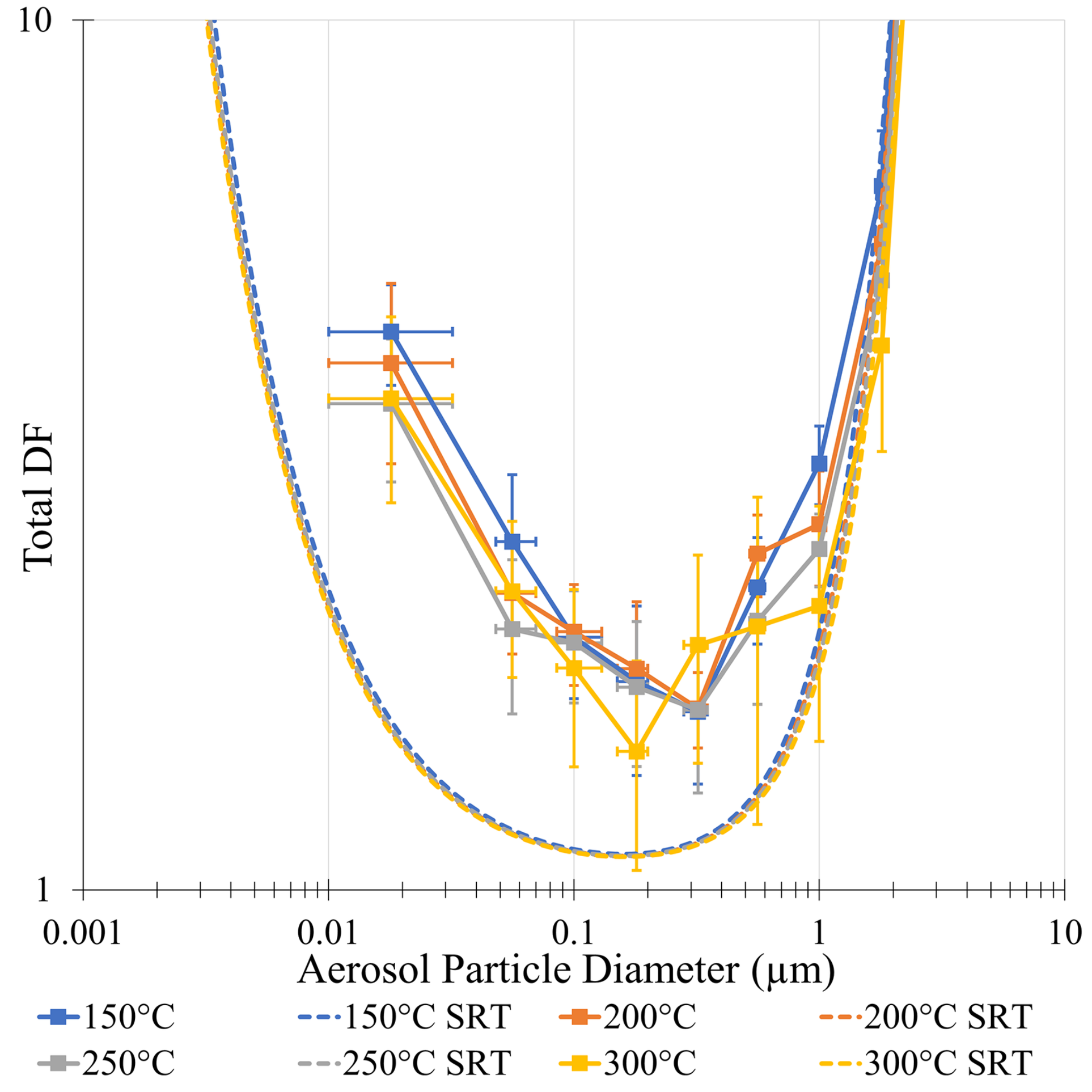
10
1
Total DF
0.001
0.01
0.1
1
10
Aerosol Particle Diameter (µm)
150°C
150°C SRT
200°C
200°C SRT
250°C
250°C SRT
300°C
300°C SRT

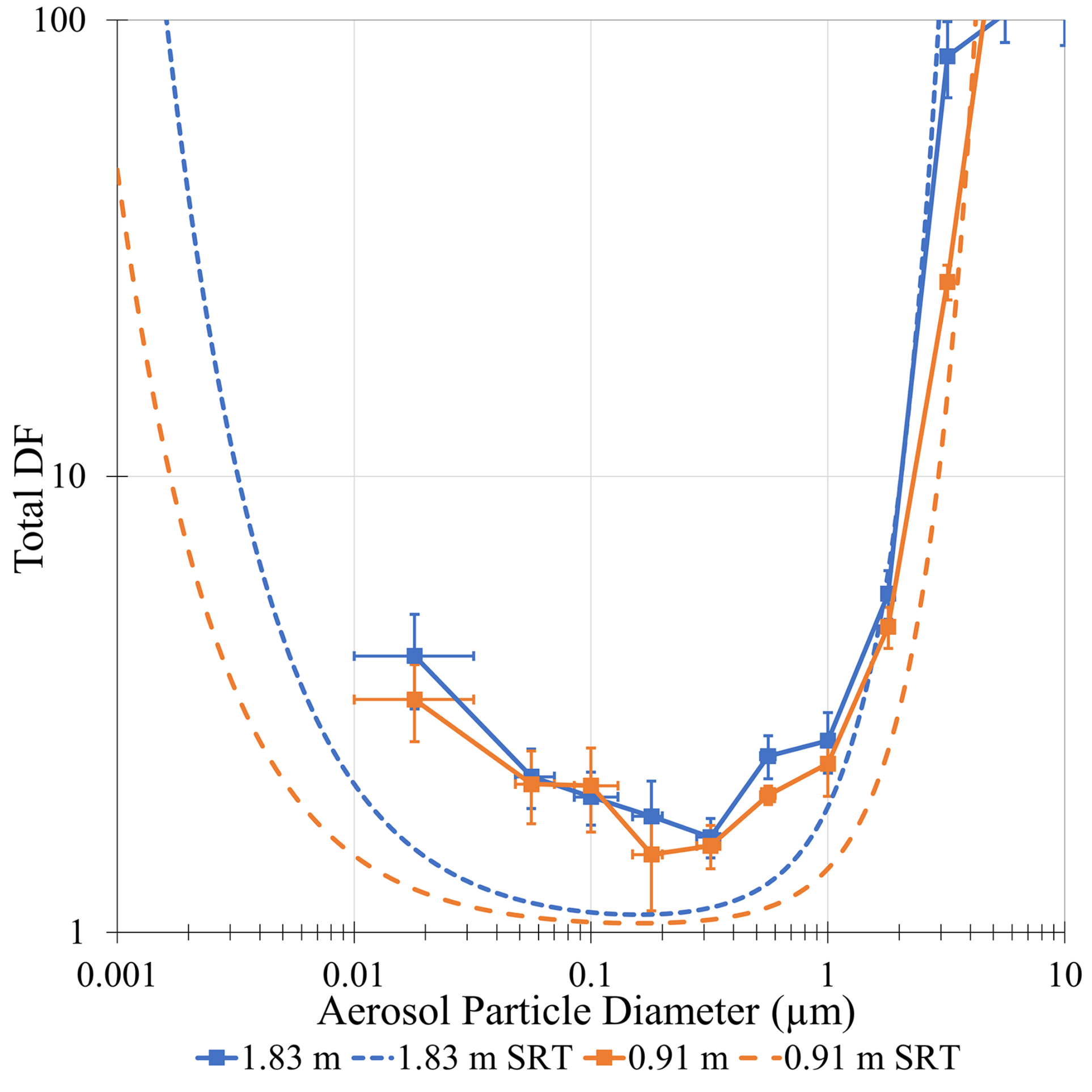
100
10
1
Total DF
0.001
0.01
0.1
1
10
Aerosol Particle Diameter (µm)
1.83 m
1.83 m SRT
0.91 m
0.91 m SRT

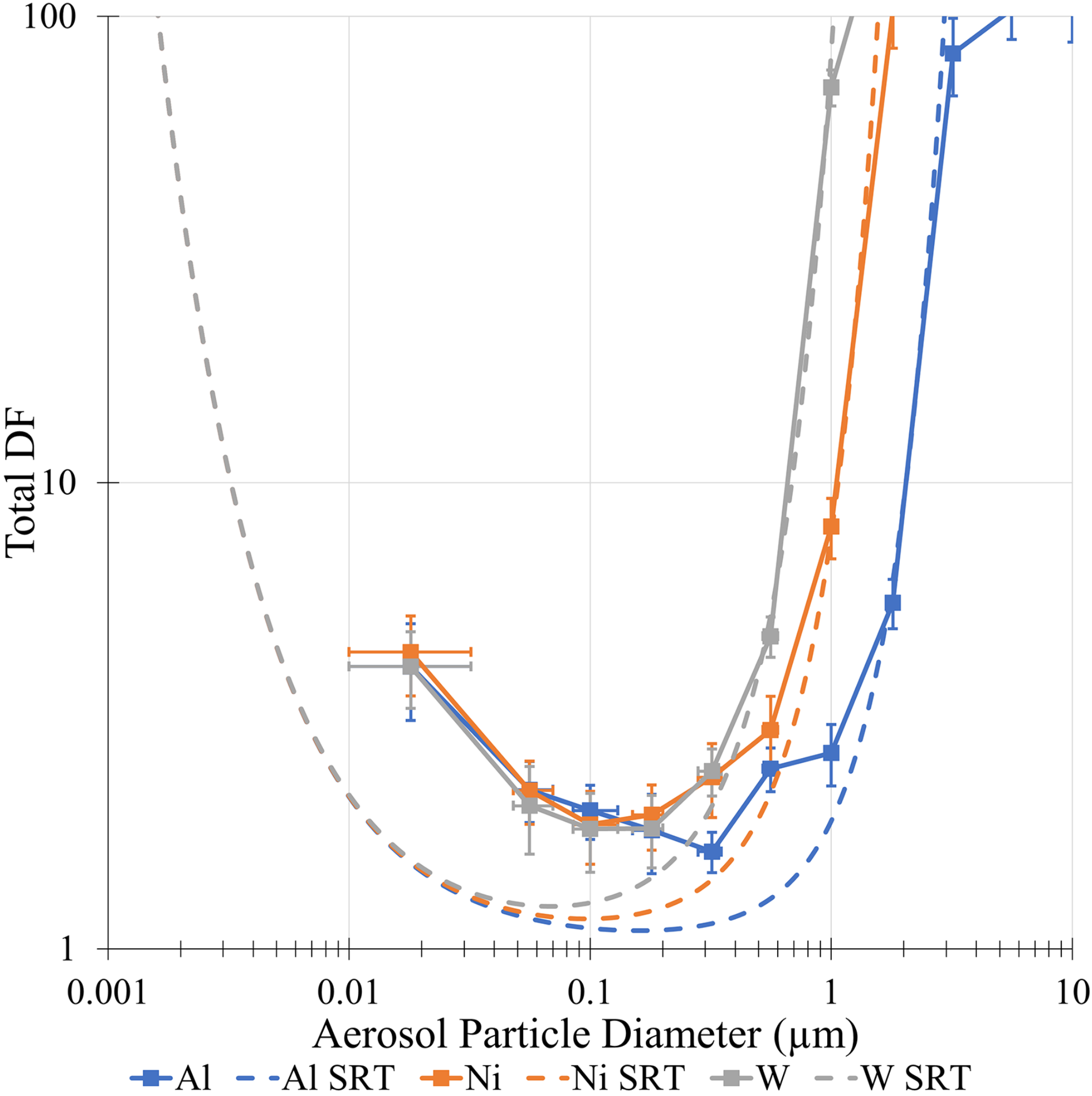
100
10
1
Total DF
0.001
0.01
0.1
1
10
Aerosol Particle Diameter (µm)
Al
Al SRT
Ni
Ni SRT
W
W SRT

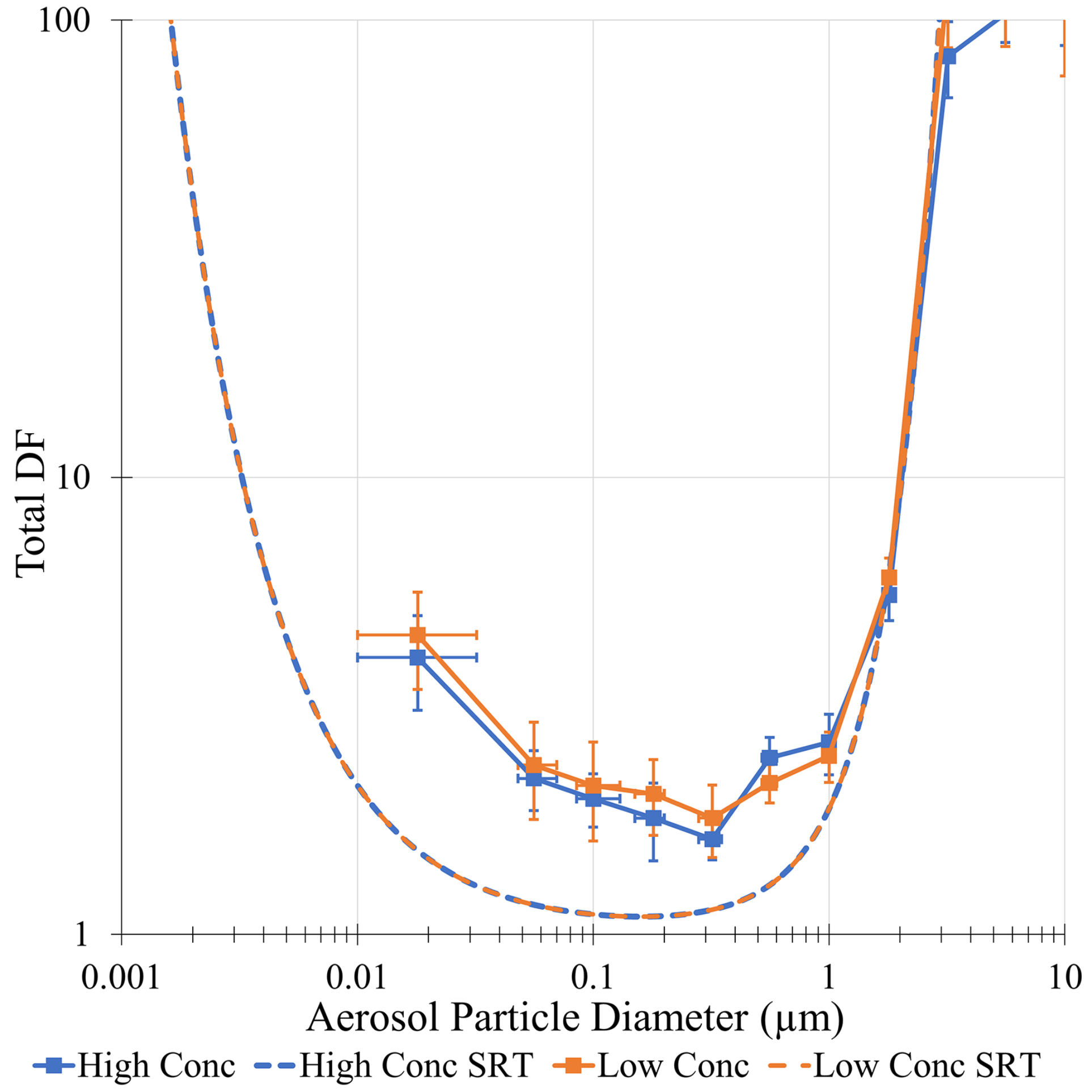
100
10
1
Total DF
0.001
0.01
0.1
1
10
Aerosol Particle Diameter (µm)
High Conc
High Conc SRT
Low Conc
Low Conc SRT

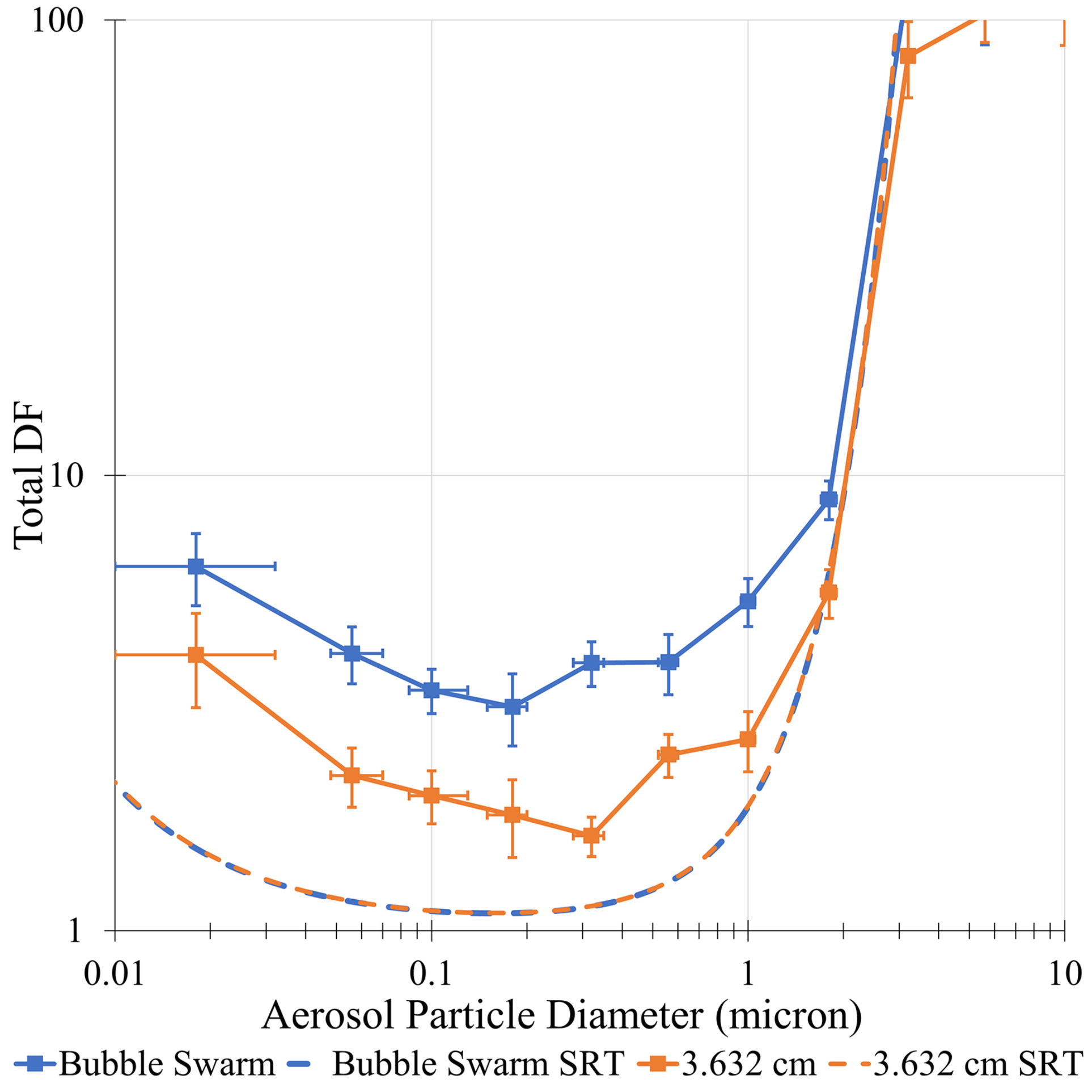
100
10
1
Total DF
0.01
0.1
1
10
Aerosol Particle Diameter (micron)
Bubble Swarm
Bubble Swarm SRT
3.632 cm
3.632 cm SRT

Nomenclature

A	Projected area $[m^2]$
C	Cunningham slip correction $[-]$
C_s	Slip correction factor $[-]$
Cal	Calibration test $[mg]$
CL	Percent of collection system losses $[-]$
d_a	Aerosol particle diameter $[m]$
d_e	Equivalent diameter of a spherical bubble $[m]$
D_b	Average bubble diameter $[m]$
DF	Overall decontamination factor $[-]$
DF_i	Decontamination factor associated with individual removal mechanisms $[-]$
E	Bubble eccentricity $[-]$
Eo	Eötvös number $[-]$
F	Volume fraction of inlet gas which condenses $[-]$
g	Gravitational acceleration $[m/s^2]$
H_p	Initial bubble submergence depth $[m]$
IL	Percent of injection losses $[-]$
K	Boltzmann constant = $1.3807x10\text{^} - 23\ J/K$
M	Morton number $[-]$
Scr	Scrubbing test $[mg]$
$SV_{crossflow}$	Sodium vapor due to crossflow only $[mg/s]$
SV_{bubble}	Sodium vapor due to bubble flow only $[mg/bubble]$
T_B	Bubble bulk gas temperature $[K]$
U_B	Bubble rise velocity $[m/s]$
v_b	Terminal rise velocity of bubble $[m/s]$
V_0	Average velocity at nozzle exit $[m/s]$
W	Nozzle diameter $[m]$

Greek symbol

α_i	Rate of aerosol scrubbing by individual removal mechanism $[1/m]$
μ_g	Gas viscosity $[m^2/s]$
μ_l	Liquid viscosity $[m^2/s]$
ρ_a	Density of aerosol particle $[kg/m^3]$
ρ_l	Density of liquid $[kg/m^3]$
ρ_p	Density of aerosol particle $[kg/m^3]$
σ_l	Surface tension of liquid-gas interface $[N/m]$

Subscript

C	Condensation removal mechanism
D	Brownian diffusion removal mechanism
S	Gravitational sedimentation removal mechanism
I	Inertial deposition removal mechanism

Table I: Bubble Characteristics

Pool Temperature	°C	200				150	250	300
Equivalent Bubble Diameter	cm	2.36	2.86	3.63	4.11	3.28	3.86	4.12
Rise Velocity	m/s	0.41	0.42	0.45	0.49	0.46	0.48	0.47
Eccentricity	-	3.11	3.62	3.67	3.76	3.56	3.88	3.98

Table II: Testing Parameter Values

Parameters	Units				
Particle Size	(μm)	0.01-18			
Bubble Size	(cm)	2.36	2.86	3.63	4.11
Pool Temperature	(°C)	150	200	250	300
Aerosol Concentration	(g/m^3)	15.3		5.4	
Pool Depth	(m)	1.83		0.91	
Particle Density	(g/cm^3)	2.7	8.9	19.3	